Physics in Medicine & Biology

ACCEPTED MANUSCRIPT

Optoacoustic image formation approaches - a clinical perspective

To cite this article before publication: Xose Luis Dean-Ben *et al* 2019 *Phys. Med. Biol.* in press https://doi.org/10.1088/1361-6560/ab3522

Manuscript version: Accepted Manuscript

Accepted Manuscript is "the version of the article accepted for publication including all changes made as a result of the peer review process, and which may also include the addition to the article by IOP Publishing of a header, an article ID, a cover sheet and/or an 'Accepted Manuscript' watermark, but excluding any other editing, typesetting or other changes made by IOP Publishing and/or its licensors"

This Accepted Manuscript is **© 2019 Institute of Physics and Engineering in Medicine**.

During the embargo period (the 12 month period from the publication of the Version of Record of this article), the Accepted Manuscript is fully protected by copyright and cannot be reused or reposted elsewhere.
As the Version of Record of this article is going to be / has been published on a subscription basis, this Accepted Manuscript is available for reuse under a CC BY-NC-ND 3.0 licence after the 12 month embargo period.

After the embargo period, everyone is permitted to use copy and redistribute this article for non-commercial purposes only, provided that they adhere to all the terms of the licence https://creativecommons.org/licences/by-nc-nd/3.0

Although reasonable endeavours have been taken to obtain all necessary permissions from third parties to include their copyrighted content within this article, their full citation and copyright line may not be present in this Accepted Manuscript version. Before using any content from this article, please refer to the Version of Record on IOPscience once published for full citation and copyright details, as permissions will likely be required. All third party content is fully copyright protected, unless specifically stated otherwise in the figure caption in the Version of Record.

View the article online for updates and enhancements.

This content was downloaded from IP address 146.107.3.4 on 07/08/2019 at 09:03

Optoacoustic image formation approaches - a clinical perspective

Xosé Luís Deán-Ben[1,2] and Daniel Razansky[1,2*]

[1]*Faculty of Medicine and Institute of Pharmacology and Toxicology, University of Zurich, Switzerland*
[2]*Institute for Biomedical Engineering and Department of Information Technology and Electrical Engineering, ETH Zurich, Switzerland*
[*] E-mail: daniel.razansky@uzh.ch

Abstract

Clinical translation of optoacoustic imaging is fostered by the rapid technical advances in imaging performance as well as the growing number of clinicians recognizing the immense diagnostic potential of this technology. Clinical optoacoustic systems are available in multiple configurations, including hand-held and endoscopic probes as well as raster-scan approaches. The hardware design must be adapted to the accessible portion of the imaged region and other application-specific requirements pertaining the achievable depth, field of view or spatio-temporal resolution. Equally important is the adequate choice of signal and image processing approach, which is largely responsible for the resulting imaging performance. Thus, new image reconstruction algorithms are constantly evolving in parallel to the newly-developed set-ups. This review focuses on recent progress on optoacoustic image formation algorithms and processing methods in the clinical setting. Major reconstruction challenges include real-time image rendering in two and three dimensions, efficient hybridization with other imaging modalitites as well as accurate interpretation and quantification of bio-markers, herein discussed in the context of ongoing progress in clinical translation.

I. INTRODUCTION

Rapid technological developments over the last decade have contributed to a wide adoption of optoacoustic (OA) imaging methods in biomedical research in areas such as neuroscience, cancer and metabolic research or cardiovascular biology, to name a few examples [1-6]. One of OA's main advantages is its unique label-free anatomical and functional contrast [7]. Endogenous contrast is mainly provided by hemoglobin, which facilitates angiographic imaging and oxygen saturation mapping at scales ranging from single capillaries to major blood vessels, e.g. the carotid artery [8-11]. Other endogenous chromophores mainly absorbing at longer (near-infrared (NIR)) wavelengths, such as lipids and water, provide additional opportunities for label-free characterization of atherosclerotic plaques [12, 13], fatty liver [14] or lipomas [15]. These unique advantages initially demonstrated in preclinical studies have fostered clinical translation of the OA modality, with promising results obtained in patients with breast cancer [16-19], inflammatory bowel (Crohn's) disease [20], thyroid cancer [21], skin conditions [22, 23] or peripheral vascular diseases [24].

Typical penetration depth of OA tomography is sufficient for whole-body imaging of rodents and smaller animals [25, 26]. However, the range of potential human application is mainly limited to superficial areas up to a depth of several centimeters, depending on the excitation wavelength and imaged tissue. Yet, deeper regions can be reached using endoscopic or intravascular approaches. Hand-held operation is a key advantage when it comes to routine clinical use of an imaging instrument as it allows for portability and rapid bed-side diagnosis. Handheld OA probes enable the visualization of tissues in real-time, similarly to the widely-employed ultrasound (US) scanners, and can operate as stand-alone systems [27-29] or be hybridized with ultrasonography [30-34]. Endoscopic and intravascular probes have been used to reach internal organs [35-37], which can also be combined with US or other optical imaging modalities [38-40]. Alternatively, imaging systems based on scanning one or several US transducers have been developed. Those range from high resolution scanners that can map microvascular structures in the skin [23] to large-scale systems covering extensive volumes, such as the entire female breast [10].

Accepted Manuscript

In addition to the hardware components of the imaging system, reconstruction and processing algorithms play an equally important role in achieving optimal imaging performance. In general, image formation in OA relies both on the physical arrangement of US detectors and light guiding elements as well as on mathematical algorithms that transform the information encoded in the signal domain (time-resolved sinograms) into the image domain (two- or three-dimensional distribution of the absorbed optical energy) [41]. In some cases, OA image can be readily obtained by stacking up (superimposing) the acquired raw signals, as in the case of optical-resolution OA microscopy where a focused light beam is raster-scanned along the surface tissue surface [42]. However, accurate reconstruction algorithms are essential for image formation in tomographic imaging approaches where the achievable resolution, signal quantification and overall image quality would largely hang upon optimal reconstruction methodology. Overall, a trade-off may generally exist between imaging performance and computational complexity of the reconstruction method. Advanced algorithms have been developed to account for the response of US sensors [43-45], speed of sound differences [46-49], light fluence variations [50-53], acoustic attenuation [54-56] or acoustic reflections and scattering [57, 58]. Most of these algorithms are however relatively slow, and simplified approaches are usually preferred for attaining real-time visualization [59], an important prerequisite for efficient use during clinical interventions.

This paper reviews the OA image formation methodologies that find applicability in the clinical setting. Existing hardware configurations are covered along with the associated signal and image processing approaches. The performance of image reconstruction algorithms is discussed in the context of emerging clinical applications.

II. GENERAL CONSIDERATIONS

Efficient clinical translation commonly implies an *ad-hoc* design with performance tailored to the specific application of interest. In human imaging applications, the technical considerations may substantially differ from typical small animal imaging scenarios. Of particular importance are the laser safety considerations. The American National Standards Institute (ANSI) has established maximum permissible exposure (MPE) limits for laser irradiation of the skin [60]. OA imaging is generally based on short-pulsed laser excitation. Hence, two specific limits need to be met, namely the per-pulse energy density as well as the mean light intensity. Both limits are wavelength dependent as plotted in Fig. 1a for typical nanosecond-duration pulses. For visible wavelengths below 700 nm, constant limits of 20 mJ/cm^2 and 200 mW/cm^2 are established, while these are progressively increased for longer wavelengths reaching 100 mJ/cm^2 and 1 W/cm^2 at 1050 nm. As a result, continuous exposure of the same region at the maximum per-pulse energy is only allowed at laser pulse repetition frequencies (PRF) below 10 Hz in order to conform to the mean power density limits.

Another important aspect is the selection of the optimal wavelength(s) for achieving the desired diagnostic outcome. In this regard, the general aim is to provide sufficiently high signal-to-noise ratio (SNR) when imaging at the desired depth while conforming to safety standards for laser exposure at the skin surface. In the visible and near-infrared spectra, the main endogenous absorbing molecules in biological tissues are hemoglobin, melanin, lipids and water [7]. Fig. 1b shows the optical absorption spectrum of these substances for typical concentrations in tissues and blood vessels. Due to the high concentration of hemoglobin in blood, OA naturally finds its broadest applicability as an angiographic imaging tool [61]. The absorption of hemoglobin is more than an order of magnitude higher at visible wavelengths (<650 nm) as compared to the so-called NIR window (650-1350 nm). Considering that the same safety exposure limits apply for any wavelength below 700 nm, strongest signals from living mammalian tissues are generated at wavelengths corresponding to peak absorption values of hemoglobin in the visible range. Fig. 1c shows the absorption coefficient of water and hemoglobin at typical average concentrations in soft tissues normalized with relative exposure limits at different wavelengths. However, the strong light absorption, along with optical scattering, is also associated with rapid light attenuation in biological tissues at the visible wavelengths [62]. The typical dependence of optical scattering with wavelength is further plotted in Fig. 1c. Both absorption and scattering are reduced for NIR wavelengths while water becomes highly absorbing at longer wavelengths. NIR wavelengths hence enable minimizing light attenuation in biological tissues while maximizing the achievable depth. In many cases, multiple wavelengths are required to fully exploit the spectroscopic differentiation capacity of OA imaging. Multi-spectral OA tomography (MSOT) has thus enabled resolving (unmixing) the distribution of spectrally-distinctive substances as well as rendering functional information by mapping tissue oxygen saturation [29, 63]. The wavelength dependence of light attenuation is known to cause distortion of the spectral profiles in the reconstructed images which can significantly compromise performance of spectral unmixing algorithms [64]. This effect is particularly prominent if the wavelengths are selected over wide spectral range exhibiting significant variations of the chromophore

Accepted Manuscript

absorption profiles. Thereby, for more accurate spectral differentiation it is generally preferable to use a set of wavelengths for which light attenuation does not substantially change.

Another important system design consideration is accessibility of the imaged area. Even in the NIR, light intensity attenuates by approximately an order of magnitude per centimeter [62], which restricts the achievable penetration depth to a few centimeters from the closest tissue surface. The spatial distribution of the US detecting elements must also be carefully considered. Generally, acoustic attenuation is lower than optical attenuation for detection frequencies below 20-30 MHz [54], thus the effective imaging depth is mainly limited by the light penetration. Nevertheless, it has been theoretically established and experimentally verified that accurate OA tomographic reconstructions can only be achieved when an angle of at least 180° around the region of interest (ROI) is covered by the US detectors [65-68]. Since this requirement cannot be met when imaging deep human tissues, the so-called limited-view artefacts inevitably appear in the reconstructed OA images [69]. The presence of bones, lungs or other organs exhibiting strong acoustic mismatch can also limit the ability to render images from certain regions. Due to the larger dimensions, acoustic attenuation and refraction is significantly stronger in human bones as compared to small animals, which may significantly deteriorate transcranial OA imaging performance [70, 71] or cause strong arc-type artefacts in OA tomographic reconstructions [58, 72, 73].

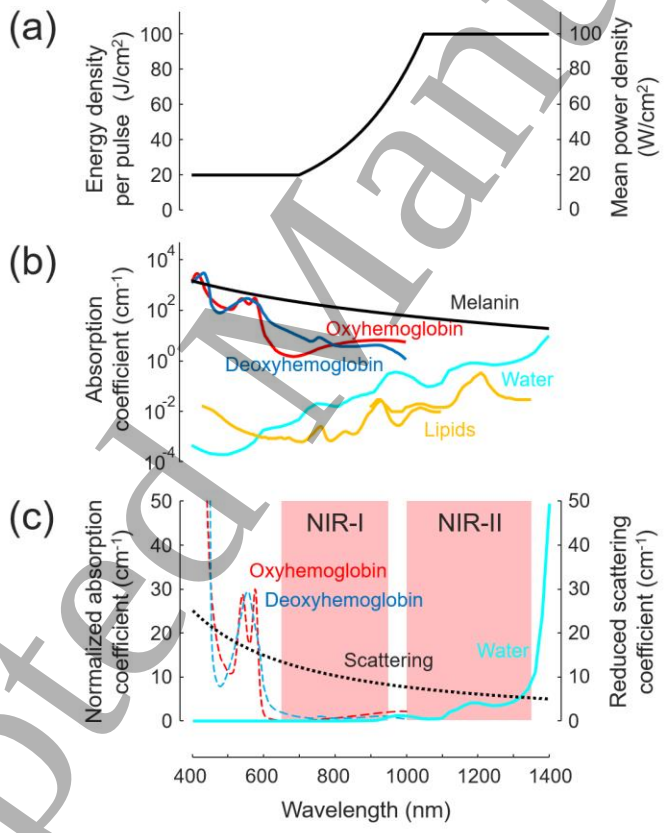


Figure 1: General considerations pertaining optoacoustic signal generation in the clinical settings. (a) Maximum permissible exposure limits as a function of wavelength according to safety standards. (b) Absorption coefficient of major endogenous chromophores at typical concentrations in mammalian tissues. Melanin (black) for typical concentrations in the skin [74], hemoglobin (red – oxygenated, blue – deoxygenated) for typical concentrations in whole blood [75], water (cyan) for a typical concentration of 80% by volume in soft tissues [76] and lipids (orange) for a concentration of 20% by volume [77, 78]. (c) Absorption coefficient of water (cyan) and hemoglobin (dashed red – oxygenated, dashed blue – deoxygenated) at typical average concentrations in soft tissues (80% and 10% by volume of water and blood, respectively [79]) normalized with relative exposure limits. The reduced scattering coefficient for average tissues is also shown (black dashed line).

III. THE OPTOACOUSTIC FORWARD PROBLEM

Accepted Manuscript

OA signals are generated via thermoelastic excitation by absorption of pulsed or modulated light, where sharp variations in light intensity maximize the conversion efficiency from optical into acoustic energy [80, 81]. Short-pulsed lasers in the nanosecond range are most commonly employed in biomedical OA imaging owing to their high OA signal generation efficiency [82]. When the laser pulse is short enough to fulfill both the stress and thermal confinement conditions (nanosecond pulse durations), the generated pressure wave field can be expressed as a function of space $\boldsymbol{r}$ and time t for an acoustically-uniform and non-attenuating medium via [83]

$$p(\boldsymbol{r},t) = \frac{1}{4\pi c}\frac{\partial}{\partial t}\frac{1}{ct}\int_{S(\boldsymbol{r},t)} p_0(\boldsymbol{r}')d\boldsymbol{r}', \quad (1)$$

where c is the speed of sound and $p_0(\boldsymbol{r}')= \Gamma(\boldsymbol{r}')\mathrm{H}(\boldsymbol{r}')$ is the initial OA pressure, being $\mathrm{H}(\boldsymbol{r}')$ the absorbed energy per unit volume in the tissue and $\Gamma(\boldsymbol{r}')$ the dimensionless Grüneisen parameter. The integral in Eq. 1 is performed along a spherical surface $S(\boldsymbol{r},t)$ with radius $|\boldsymbol{r}'-\boldsymbol{r}|=ct$. In some cases, dimensionality of the OA forward model can be reduced. For instance, if the OA sources are confined in a cross-sectional plane (2D), Eq. 1 can be simplified (in arbitrary units) to

$$p(\boldsymbol{r},t) = \frac{\partial}{\partial t}\frac{1}{t}\int_{L(\boldsymbol{r},t)} p_0(\boldsymbol{r}')d\boldsymbol{r}'. \quad (2)$$

In this case $L(\boldsymbol{r},t)$ is an arc with radius $|\boldsymbol{r}'-\boldsymbol{r}|=ct$. If the OA problem is confined to a line (1D case), Eq. 2 can be further simplified (in arbitrary units) to express the pressure field $p(x,t)$ at an arbitrary point along such line as

$$p(x,t) = \frac{\partial}{\partial t}\frac{1}{t}p_0(x+ct), \quad (3)$$

being ct the distance from the point at which the pressure field is considered. The OA sources are approximately confined to a line e.g. when using a light excitation beam coaxially aligned with an ultrasound transducer as described in section IV.

The collected OA signals are further affected by the so-called electrical impulse response $EIR(t)$ of the US sensor(s). Moreover, most detectors have a finite size that results in them having a spatially-dependent spatial impulse response $SIR(\boldsymbol{r}',t)$. The collected signal $s(r_0,t)$ by a finite-size transducer located at r_0 and perfectly matched to the coupling medium can be assumed to be proportional to the integral of the pressure on the active surface $A(\boldsymbol{r})$ [84]. Hence, it can be expressed (in arbitrary units) as

$$s(r_0,t) = EIR(t) * \int_{A(\boldsymbol{r})} p(\boldsymbol{r},t)d\boldsymbol{r}, \quad (4)$$

where * denotes convolution. For an OA pressure signal at r_0 generated at $\boldsymbol{r}'$, denoted $p_{\boldsymbol{r}'}(r_0,t)$, Eq. 4 can equivalently be expressed as [45]

$$s(r_0,t) = EIR(t) * SIR(\boldsymbol{r}',t) * p_{\boldsymbol{r}'}(r_0,t). \quad (5)$$

OA image formation approaches are generally based on the models defined in Eqs. 1-5. More sophisticated models exist e.g. to further account for acoustic attenuation or speed of sound variations. In the following sections, we describe the application of such models for the commonly employed OA imaging embodiments.

IV. OPTOACOUSTIC MICROSCOPY

The first OA images that found applicability in biological research were acquired by scanning a single-element transducer either around or across the sample [85, 86]. While tomographic scanning trajectories based on signal acquisition at several angular positions have progressively been substituted by transducer arrays [87-91], single-element scanning approaches have retained their relevance, also for clinical translation [23, 92]. Due to their tight acoustic or optical focusing, the optoacoustic microscopy (OAM) techniques attain generally higher spatial resolution than their tomographic counterparts and usually operate within microscopic to mesoscopic depths of up to several

Accepted Manuscript

millimeters within living tissues. OAM is classified into two groups, namely optical-resolution and acoustic-resolution methods, depending on the type of focusing employed.

Optical-resolution OAM (OR-OAM) is based on focusing light onto the region of interest and collecting the generated signals with an ultrasound transducer coaxially aligned with the light beam [93]. This can be achieved by either guiding light through an aperture in the transducer or by using acoustic mirrors (Fig. 1a). In this way OR-OAM is capable of resolving superficial microvascular structures. Since the illuminated spot is being rapidly scanned, only the maximum per-pulse energy density is of relevance for the laser safety considerations under these conditions. As an example, Fig. 1b shows an image of the human cuticle microvasculature being acquired with OR-OAM. Capillary loops can easily be distinguished in the single-wavelength images and the oxygen saturation can further be characterized from multi-spectral measurements [92]. Fig. 1c displays the OR-OAM image of rabbit's retina [94], which suggests potential clinical applicability of OA in ophthalmology. However, more restrictive safety exposure limits must be observed when exposing the human retina to pulsed light [60]. In OR-OAM, the depth is encoded in the time-resolved OA signals via ultrasound time-of-flight. 2D or 3D image formation is then based on stacking the processed signals. The lateral resolution is determined by the size of the light focus, typically in the order of a few micrometers [95], which can further be improved with super-resolution approaches [96]. Similarly to other optical microscopy methods using focused light beams, OR-OAM is only applicable for depths <1 mm within scattering biological tissues. For each detector position, the OA forward model can be approximated by the 1D case in Eq 3. Considering a point transducer aligned with the optical beam, Eq. 5 can then be expressed as

$$s(x_0, t) = EIR(t) * \frac{\partial}{\partial t}\frac{1}{t} p_0(x_0 + ct). \qquad (6)$$

Eq. 6 indicates that the axial resolution is associated with the bandwidth of the collected signals and can be recovered via suitable post-processing. As an example, Fig. 1d shows a comparison of the images obtained with the envelope of the acquired time-resolved signals estimated as the modulus of the corresponding analytic signals versus Wiener deconvolution of the original signals [97]. Note that the modulus of the analytic signal is generally estimated with the Matlab function *abs(hilbert)* and is sometimes referred to as the Hilbert transform. By definition, the Hilbert transform however corresponds to the imaginary part of the analytic signal. It is shown that deconvolution can significantly enhance the axial resolution. Another important issue to consider in OR-OAM is the limited capability to visualize objects oriented along the imaged axis. The derivative term in Eq. 6 indicates that prominent signals are produced at the edges of structures being excited with the focused light beam, and hence mainly such boundaries appear in the images. The visible boundaries of an object are determined by the range of angles covered by the points at which signals are collected. Thus, elongated structures aligned with the excitation light beam, as is the case of vertical blood vessels, are generally missed in OR-OAM images. These so-called limited view effects can be mitigated by considering different illumination angles and optical focus dimensions [98]. For example, the 1D model in Eq. 6 is no longer valid for a light beam with a small depth of field. Indeed, the non-uniform light intensity within the beam results in less prominent signals generated at the edges and hence the visibility of entire structures is expected to be enhanced. Fig. 1e shows a comparison between OR-OAM images acquired with optical objectives with different numerical apertures [98]. Clearly, visibility of structures is enhanced for larger numerical apertures, which comes to the detriment of the effective depth of focus.

Accepted Manuscript

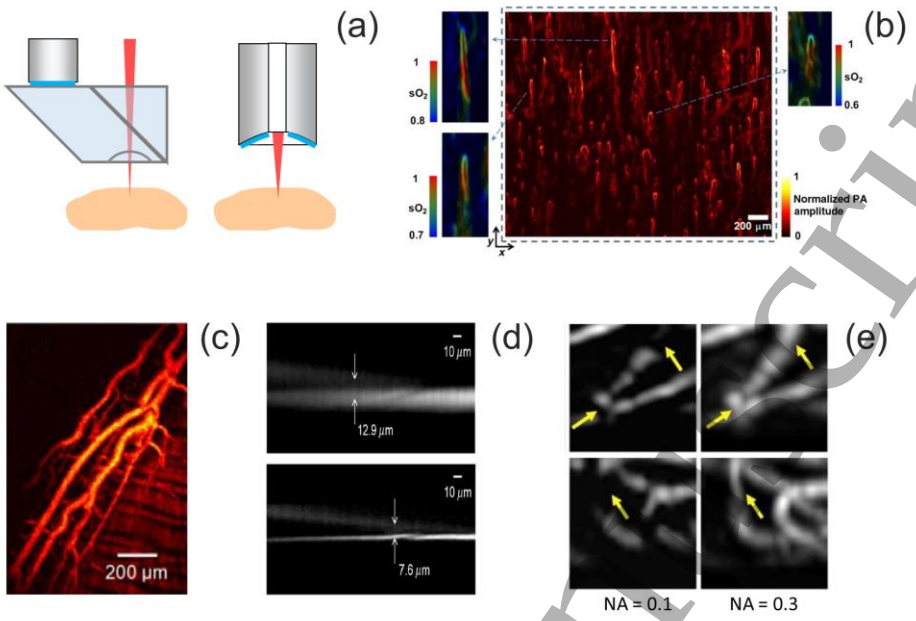


Figure 2: Optical-resolution optoacoustic microscopy (OR-OAM). (a) Lay-out of exemplary systems based on raster-scanning the light beam (left) and the ultrasound transducer (right); blue – sensing surface of the ultrasound transducer, red – light beam. (b) OR-OAM image of the human cuticle microvasculature [92]. (c) OR-OAM image of the rabbit retina [94]. (d) Axial resolution enhancement after Wiener deconvolution (bottom) with respect to the original images (top) [97]. (e) Comparison of the limited-view effects for OR-OAM images acquired with optical objectives with different numerical aperture (NA) [98].

Acoustic-resolution OAM (AR-OAM) relies on an axially-symmetric ultrasound transducer to selectively detect optoacoustic signals generated along its "line of sight" [99]. Generally, this is achieved with spherically-focused transducers that are used with different illumination strategies (Fig. 2a). Unlike OR-OAM, the AR-based techniques are not directly affected by light scattering and hence can image regions beyond the light diffusion limit. The availability of single-element ultrasound detectors covering a large range of frequencies makes AR-OAM particularly suitable for multi-scale imaging, operating at various scales, from macroscopic structures [86] to capillaries [23] to individual cells [100]. Much like OR-OAM, the AR-OAM techniques can be used for the characterization of microvascular structures in the clinical setting. The energy per pulse must equally be observed [60]. Moreover, due to its deeper penetration, AR-OAM commonly employs higher per-pulse energy and hence broader (unfocused) illumination that largely overlaps for the different scanning positions. Hence, the mean laser intensity is of relevance for the safety limits. Fig. 2b shows a comparison of the images of healthy and psoriatic skin acquired with raster-scan optoacoustic mesoscopy (RSOM), a particular implementation of AR-OAM, which has shown promise for high-resolution imaging of microcirculation and layers of the human skin [23]. To this end, RSOM facilitated label-free visualization of inflammation and psoriasis-related biomarkers, while its advantages can be expanded to other dermatologic conditions [101].

A particularly important aspect to consider is the rapid signal decay with depth that occurs due to both light and ultrasound attenuation in tissues. The latter is generally weaker for ultrasound frequencies below 20-30 MHz but becomes dominant at higher frequencies [54]. Optical attenuation further has a strong wavelength dependence with the light absorption by blood being more than an order of magnitude higher at visible wavelengths as compared to the NIR spectrum, the latter predominantly used for deep-tissue imaging [62]. In principle, volumetric images in AR-OAM can be rendered similarly to OR-OAM, i.e. by stacking the A-mode signals [102]. In this way 3D vasculature structure can be resolved (Fig. 2c), albeit discontinuities in blood vessels are clearly manifested due to the previously mentioned limited-view effects. The axial resolution in AR-OAM is determined by the detector bandwidth while the lateral resolution at the focal plane is further affected by the numerical aperture of the spherically focused transducer [42]. The lateral resolution can severely deteriorate in areas lying outside the focal plane if the recorded time-resolved A-lines are simply stacked for image formation. According to Eq. 4, the lateral resolution at locations away from the focal plane can be generally improved by combining the information from several scanning positions. For this, one

Accepted Manuscript

may use simplified methods based on an *a-priori* known transducer sensitivity field, such as virtual detector or synthetic aperture focusing techniques (SAFT) [103-105]. Results of the application of different SAFT-based methods for forming AR-OAM images of point absorbers at different depths are shown in Fig. 3d. The vertical (x-direction) elongation of the absorbers in the images corresponds to the achieved lateral resolution. Clearly, the lateral resolution can be significantly enhanced with SAFT-based methods at locations away from the acoustic focus. More sophisticated approaches based on an accurate modelling of transducer's frequency dependent sensitivity are also available at the cost of a higher computational complexity [106-108]. Yet, due to the limited-view acquisition geometry, structures oriented along detector's axis remain barely visible in AR-OAM, also after application of the above reconstruction methods.

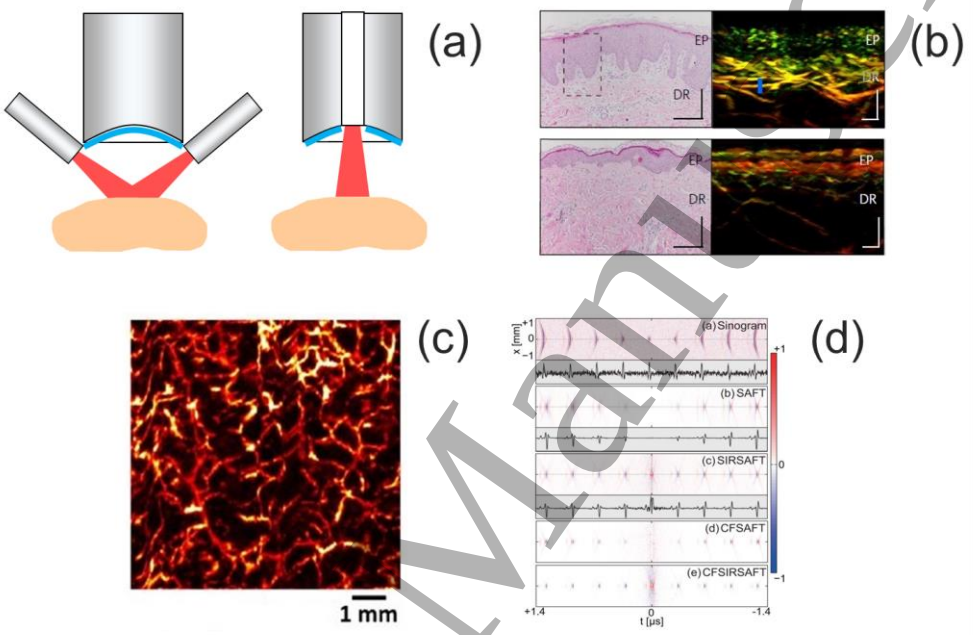


Figure 3: Acoustic-resolution optoacoustic microscopy (AR-OAM). (a) Examples of experimental embodiments; blue – sensing surface of the ultrasound transducer, red – light beam. (b) Raster-scan optoacoustic mesoscopy (RSOM) images of psoriatic (top) and healthy (bottom) skin along with the corresponding histology images (left) [23]. (c) Top projection of a volumetric AR-OAM image of a human arm [102]. (d) Lateral view of the AR-OAM images of point absorbers formed with the original sinogram and with different methods based on the synthetic aperture focusing technique (SAFT). The vertical (x-direction) elongation of the absorbers in the images corresponds to the achieved lateral resolution [104].

V. Cross-sectional hand-held imaging

At present, pulse-echo US remains the most widely employed imaging modality in the clinical practice, owing to its hand-held operation and real-time imaging performance. OA can similarly be operated in the portable mode, yet a number of fundamental differences between the two modalities need to be taken into account for efficient design of hand-held OA imaging systems. First, OA scanners based on array transducers employ a relatively broad illumination geometry that does not substantially change for consecutive frames. Hence, both the per-pulse energy density as well as the mean laser intensity must be maintained below the respective safety limits. As mentioned in section 2, when operating at the maximum permissible per-pulse energy levels, the laser PRF must be kept below 10 Hz, which is substantially lower than the typical frame rates of pulse-echo US. Hand-held OA imaging systems operating at PRFs in the order of kHz have been also developed [109-111]. However, the per-pulse energy must then be significantly reduced in order to meet the safe exposure limits on the average intensity, resulting in deterioration of the SNR and achievable penetration depth. The recorded OA responses are also significantly weaker than the reflected signals in pulse-echo US. This implies increasing the amplification and using larger size and/or more sensitive detection elements.

Accepted Manuscript

Initial implementations of cross-sectional hand-held OA imaging systems were based on linear arrays analogous to those used in pulse-echo US. Linear arrays with broad selection of central frequency are commercially available at low cost. Thus, hand-held OA imaging can readily be achieved by integrating light delivery into the imaging plane and collecting the generated responses (Fig. 4a). Variety of light sources and illumination geometries have been proposed, including tunable OPO lasers guided via fiber bundles [30], integration of laser diodes [32] or light emitting diode (LED) arrays [110, 111]. The main advantage of linear-array-based imaging systems is the ease of hybridization and co-registration between US and OA [112, 113]. OA image formation with linear arrays is generally based on delay-and-sum algorithms analogous to those used in US, where the OA image (initial pressure distribution $p_0(\boldsymbol{r})$) is reconstructed via

$$p_0(\boldsymbol{r_j}') = \sum_i s_f(\boldsymbol{r}_i, t_{ij}), \qquad (7)$$

where $\boldsymbol{r_j}'$ is image pixel, $\boldsymbol{r}_i$ is the position of a specific sensor, $t_{ij}=|\boldsymbol{r}_i-\boldsymbol{r}'_j|/c$ is the time-of-flight and $s_f(\boldsymbol{r}_j,t_{ij})$ are the acquired signals after being filtered..Examples of images rendered with this approach are shown in Fig. 4b [30]. Three-dimensional images can also be formed by simply stacking the reconstructed cross-sections (Fig. 4c) [114]. However, Eq. (7) represents a purely heuristic approach for OA image reconstruction. Thus, the images are not expected to accurately represent distribution of the optical absorption in the imaged tissue. Even though more sophisticated approaches, e.g. based on focal-line 3D image reconstruction, may slightly enhance the image quality (Fig. 4d) [115], OA images rendered with linear arrays are inevitably afflicted with limited-view artefacts [68]. Reflection artefacts and clutter represent another source of artifacts affecting the images [116], which can be dealt with by employing algorithms exploiting the combination with simultaneously acquired US information (Fig. 4e) [73].

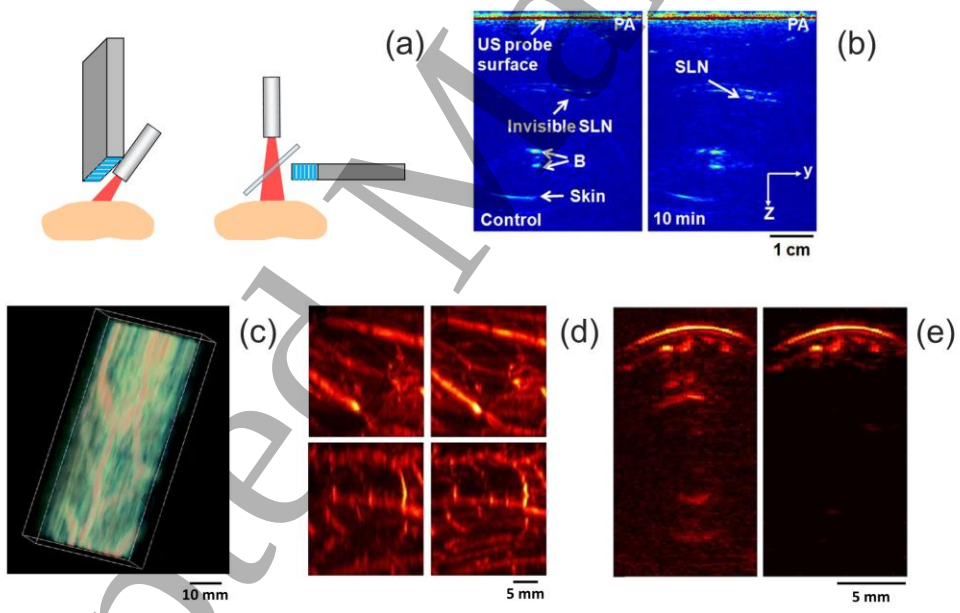


Figure 4: Cross-sectional hand-held optoacoustic tomography (OAT) based on a linear array. (a) Examples of experimental embodiments combining the ultrasound array with light delivery; blue – ultrasound array elements, red – light beam. (b) Cross-sectional images of sentinel lymph nodes before (left) and after (right) injection of methylene blue [30]. (c) Three-dimensional image of the human forearm obtained by composing cross-sectional images [114]. (d) Comparison of the three-dimensional images (top views) formed by stacking cross-sections (left) and by using the focal-line three-dimensional image reconstruction (right) [115]. (e) Reflection-artefacts in a cross-sectional image (left) being removed via multispectral analysis [73].

A more suitable approach for the implementation of OA hand-held scanners consists in adapting concave array geometry typically used in small-animal multi-spectral optoacoustic tomography (MSOT) systems [11, 27] for concurrent US imaging. A lay-out of the arrangement of illumination and detection components for this configuration is depicted in Fig. 5a. Exemplary images rendered with this approach are displayed in Fig. 5b [24]. Due to the larger angular coverage, hand-held OA scanners based on concave arrays outperform those based on linear arrays in terms

Accepted Manuscript

of signal quantification abilities and overall image quality [117]. The image quality improvement can readily be recognized when transitioning from 90° to 270° angular coverage (Fig. 5c) with a clear improvement in visibility of the vertically oriented structures [68]. In the concave geometry the array detection elements are not located in close proximity to the skin surface. Thus, the excitation light can optimally be delivered into the imaged plane, eliminating contrast deterioration due to the clutter artifacts [116]. On the other hand, the speed of sound in the coupling medium separating skin from the detection aperture may differ from that in tissues, which may lead to resolution degradation if not properly accounted for [47]. The wide use of concave arrays in small-animal MSOT imaging has fostered the development of advanced reconstruction procedures based on iterative model-based algorithms [118-121]. For this, Eq. (2) is discretized in a way that the pressure at a set of positions and instants, expressed in a vector form as $\mathbf{p}_T$, is theoretically described in a matrix form as

$$\mathbf{p}_T = \mathbf{A}\mathbf{p}_0, \qquad (8)$$

where $\mathbf{p}_0$ is the initial OA pressure at the pixels of a grid, representing the OA image in a vector form, and $\mathbf{A}$ is the model-matrix corresponding to the linear transformation in the discrete OA forward model. The OA image is then estimated via numerical minimization of the error between the measured signals at a set of points and instants, expressed in a vector form as $\mathbf{p}_m$, and the theoretical ones given by Eq. (8), i.e.,

$$\mathbf{p}_{0,\mathrm{sol}} = \mathrm{argmin}_{\mathbf{p}_0} \left\| \mathbf{p}_{0,\mathrm{sol}} - \mathbf{A}\mathbf{p}_0 \right\|_2^2 + \lambda R(\mathbf{p}_0), \qquad (9)$$

$\lambda R(\mathbf{p}_0)$ in Eq. (9) corresponds to a regularization term, which is generally required for tomographic coverage below 180° [67]. Model-based algorithms have been shown to significantly outperform delay-and-sum and backprojection methods in terms of reconstruction accuracy (Fig. 4d) [122]. The drawback of iterative reconstruction methods is their long computational time. However, a number of acceleration strategies have been developed. For instance, computation of the matrix-vector multiplications involved in the iteration procedure to solve Eq. (9) has facilitated parallel implementation on graphics processing units (GPUs) [123]. Such implementation has enabled attaining high-resolution model-based reconstructions at 20Hz frame rates, which is sufficient for providing real-time feedback in cross-sectional OA hand-held scanners operating at PRFs in the order of 10 Hz.

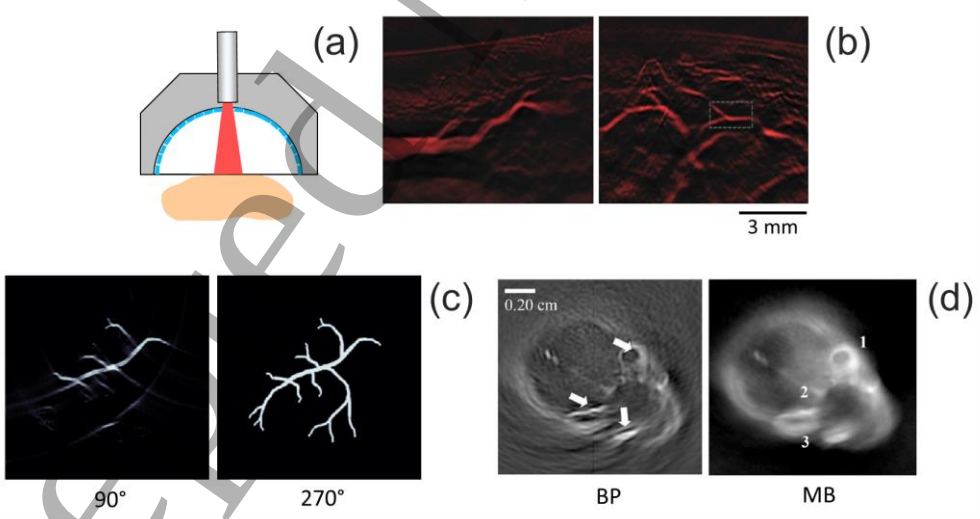


Figure 5: Cross-sectional hand-held optoacoustic tomography (OAT) based on a curved (concave) arrays. (a) Lay-out of the ultrasound array and the light delivery method; blue –ultrasound array elements, red – light beam. (b) Cross-sectional images of the medial side (left) and the distal tip (right) of the hallux [24]. (c) Effects of the angular coverage of the array on the visibility of vascular structures [68]. (d) Comparison between cross-sectional reconstructions of a mouse head obtained with back-projection (left) and model-based (right) algorithms [122].

Note that concave arrays are not readily suitable for pulse-echo US imaging, which requires the inter-element pitch to be sufficiently small to avoid image artefacts associated with high order diffraction lobes. Hybrid OA and pulse-echo US has been implemented with concave arrays having small pitch [124]. However, a relatively large number of

Accepted Manuscript

elements was required to cover the large detection angle, which increased system's complexity and cost. An alternative solution for OA/US hybridization is a multi-segment array geometry consisting of a central linear part and two lateral concave parts (Fig. 6a) [34]. For this configuration, the best performance is achieved when pulse-echo US images are formed with the signals collected with the linear array segment while all the array elements are used for the OA image formation (Fig. 6b) [125]. Optoacoustic image reconstruction can then be performed by the previously described methods but the signals need to additionally be weighted by the respective size-dependent sensitivity of the individual array elements. This new approach allows fully exploiting the optimal acquisition geometry for both modalities while simultaneously delivering their highly complementary structural and functional information [125], [126].

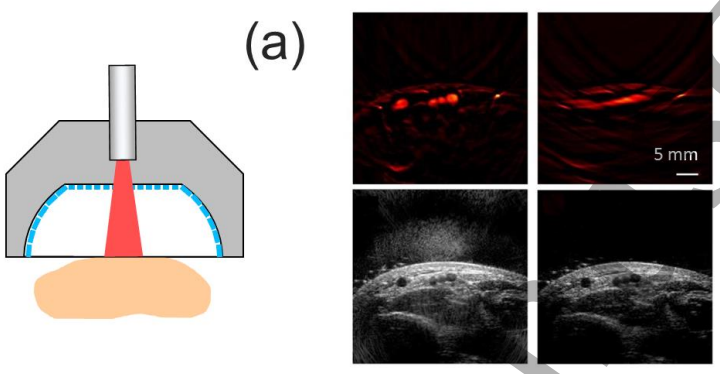


Figure 6: Cross-sectional hand-held optoacoustic tomography (OAT) based on a hybrid (multi-segment) array. (a) Lay-out of the ultrasound array and the light delivery method; blue –ultrasound array elements, red – light beam. (b) Optoacoustic (top) and ultrasound (bottom) images of the human wrist acquired when considering all the array elements (left) versus only its linear part (right) [125].

VI. Volumetric hand-held imaging

The wide adoption of B-mode US as a clinical imaging tool has fostered the extension of this modality into volumetric (3D) imaging. The so-called 3D US has been implemented by means of two dimensional (planar or convex) arrays. Similarly to the 2D case, optimal image acquisition in volumetric OA imaging implies the collection of signals from a large angular aperture surrounding the imaged object. However, truly volumetric OA imaging can significantly enhance the performance of 2D scanners by enabling proper visualization of otherwise invisible structures propagating along arbitrary directions. This is of particular importance for angiographic imaging since blood vessels correspond to elongated structures distributed in random orientations. In contrast to typical US image acquisition strategies applying line-by-line beamforming, an entire OA image volume can in principle be reconstructed with a single laser pulse. Thus, the 3D OA imaging rate is basically limited by the PRF of the laser, not by the number of A-mode signals acquired.

Customized spherical arrays with a dense distribution of unfocused detection elements have been suggested for hand-held 3D OA imaging. In analogy to pulse-echo US, 3D OA imaging in real-time can be termed 4D OA imaging [89, 127-130]. In addition, multi-spectral OA imaging further encodes information in the optical spectral domain, which effectively represents an independent dimension. State-of-the art OPO-based laser systems are capable of rapidly tuning their output wavelength on a per pulse basis at rates exceeding 100 Hz. This has turned optoacoustics into a full scale 5D imaging modality that can capture multi-spectral volumetric data from tissues in real-time with 5D standing for the three spatial dimensions, time and wavelength [131, 132]. A typical lay-out of the experimental system used for volumetric OA imaging is depicted in Fig. 7a. Image reconstruction with spherical arrays can be performed with filtered back-projection formulas derived from tomographic principles. Specifically, a universal back-projection formula exists where the initial pressure distribution can be expressed as

$$p_0(\boldsymbol{r}') = \int_{\Omega} \frac{d\Omega}{\Omega} \left[2p(\boldsymbol{r}, t) - 2t \frac{\partial p(\boldsymbol{r}, t)}{\partial t} \right]_{t=|r-r'|/c}. \qquad (10)$$

In practice, image reconstruction from a finite number of transducers is based on a discretized version of Eq. (10). The initial pressure in arbitrary units is given by

Accepted Manuscript

$$p_0(\boldsymbol{r_j}) = \sum_i p\left(\boldsymbol{r'}_i, t_{ij}\right) - t_{ij}\frac{\partial p(\boldsymbol{r'}_i, t_{ij})}{\partial t}, \qquad (11)$$

Experimentally collected data is commonly affected by the EIR of the transducer (Eq. (4)), which can be accounted for via deconvolution. Additionally, other noise reduction filters are required to remove noise, so that a filtered signal s_f is considered for the reconstruction and hence Eq. (11) is analogous to Eq. (9). Representative images of the female breast obtained with this approach are shown in Fig. 7b [133]. A larger area, such as the entire human palm, can also be covered by raster scanning the array (Fig. 7c) [134]. Overall, image reconstruction in 3D is a computationally extensive effort even when applying a simple back-projection formula. Acceleration of the reconstruction process is hence essential to ensure real-time volumetric image rendering with the spherical-array-based scanners during handheld operation in the clinics. A GPU-based implementation of Eq. (11) has been shown capable of reconstructing images consisting of approximately 10^6 voxels at rates of up to 50 frames per second [135]. Such algorithm can be modified to account for speed of sound differences between the tissue and coupling medium while still delivering real-time reconstructions (Fig. 7d) [136].

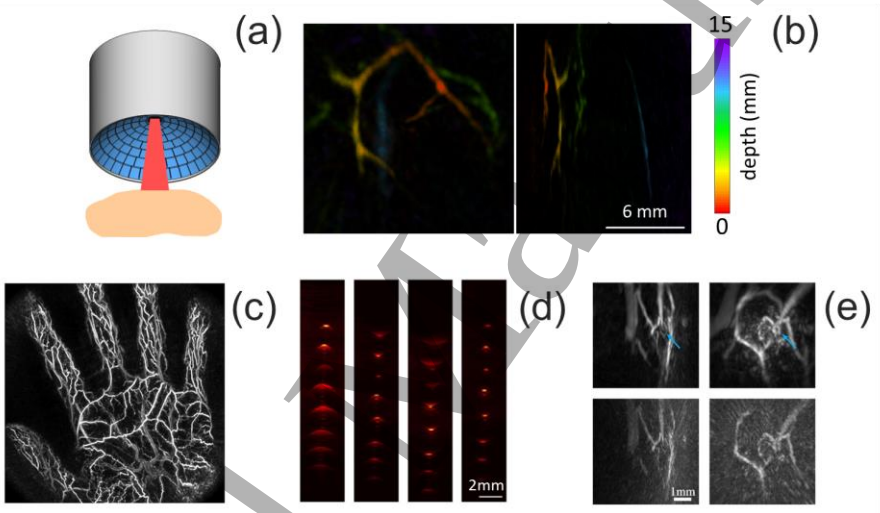


Figure 7: Three-dimensional hand-held optoacoustic tomography (OAT) based on a spherical array. (a) Lay-out of the ultrasound array and the light delivery method; blue –ultrasound array elements, red – light beam. (b) Three-dimensional optoacoustic image of the female breast color-coded for depth [133]. (c) Three-dimensional image (top view) of the human palm formed by superimposing multiple acquisitions via raster-scanning of the array [134]. (d) Comparison of the three-dimensional optoacoustic reconstructions (lateral views) of a phantom composed of absorbing spheres when considering a uniform speed of sound (first three images) and when accounting for a different speed of sound in the phantom (right-most image) [136]. (e) Comparison of the three-dimensional optoacoustic reconstructions (top views) of the human finger obtained with a 3D model-based approach accounting for the spatial impulse response of the elements (top) [137] versus filtered 3D back-projection (bottom).

More elaborate reconstruction algorithms with longer computational time can be employed off-line once the data has been acquired. For instance, model-based reconstruction algorithms can be adapted to further account for the finite aperture of the US sensing elements. This can be achieved e.g. by splitting the active area of each detection element into a set of sub-elements ΔS_i sufficiently small to be approximated as point detectors. Considering Eq. (4), the signal collected by the detector could then be approximated via

$$s(r't) \approx \sum_i p(r,t)\Delta S_i, \qquad (12)$$

and hence the equivalent model-matrix is given by

$$\mathbf{A} = \sum_i \mathbf{A}_i \Delta S_i, \qquad (13)$$

Accepted Manuscript

being $\mathbf{A}_i$ the model-matrix corresponding to each sub-set of elements. Fig. 7e demonstrates a significant image contrast and resolution improvements achieved with this approach [137] versus conventional reconstructions based on filtered 3D back-projection.

Much like in the case of cross-sectional OA scanners based on concave arrays, spherical arrays with a relatively large inter-element pitch are also not suitable for rendering pulse-echo US images. Hybridization of 4D OA hand-held imaging with US is further challenged by the relatively large acquisition time required for acquiring US images. A creative solution for attaining simultaneous 4D OA and US imaging has been proposed by using a point optical absorber as a passive source of ultrasound [138]. The collected US echoes were then processed using a delay-and-sum method analogous to Eq. (9) for concurrent rendering of 3D US images in the reflection mode.

VII. Scanning-based optoacoustic imaging

The main limitation of real-time OA imaging systems is the relatively small field of view (FOV) that can be covered in each real-time frame, typically scaling with the number of simultaneously acquired time-resolved tomographic projections [139]. The FOV can effectively be enlarged by scanning the detection array at the expense of the imaging rate. For example, whole-body imaging of mice has been achieved by translating a concave transducer array along the elevation direction [25, 88] or by helically scanning a spherical array [26, 140]. Multiple scanning-based methods have been suggested for OA imaging of relatively large areas of the human body, where the patient lies in a stationary position for typical acquisition times of several seconds to minutes.

As previously mentioned, the RSOM method has enabled high-resolution imaging of relatively large areas on the skin surface. Scanning systems are of particular importance for breast imaging applications where a large angular coverage can be achieved by properly arranging the detection positions around the breast. An example of OA human breast scanner is shown in Fig. 8a. Considering that the breast is characterized by relatively low absorption of light, angiographic imaging of a considerable portion of the breast volume has been achieved (Fig. 8b) [10]. Breast scanners based on alternative configurations have also been proposed [141, 142]. Another clinically applicable scanning-based system is based on OA signal detection with transparent Fabry Perot polymer films (Fig. 8c) [3]. Here the OA excitation is similarly provided with a broad illumination from a pulsed laser through the film. An additional focused laser beam is scanned upon the polymer film to perform point-by-point detection of the ultrasound waves over the large angular aperture representing the planar detection surface. Images of the human fingertips obtained with this system are displayed in Fig 8d [143]. High-resolution in vivo angiographic imaging has been demonstrated for depths of up to approximately 6 mm under the skin surface with this approach.

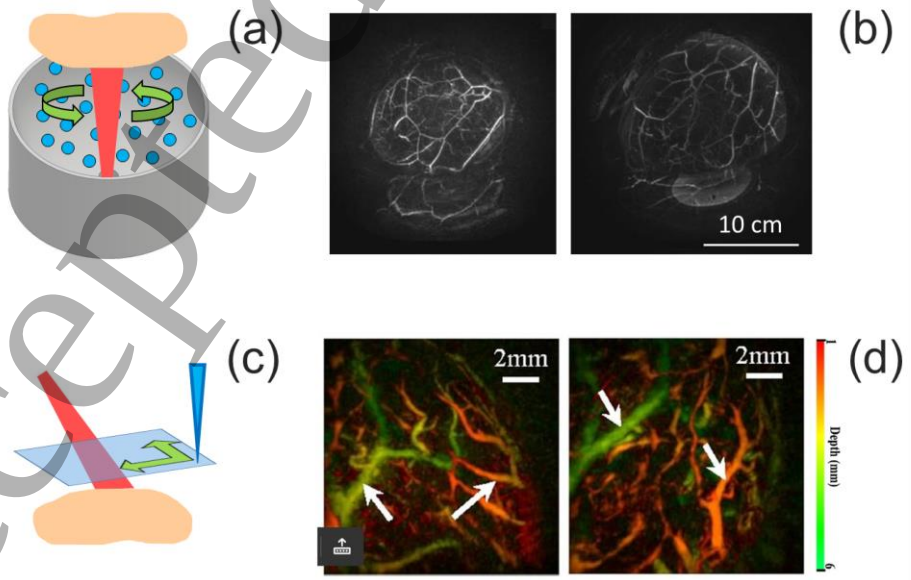


Figure 8: Three-dimensional optoacoustic tomography (OAT) based on scanning systems. (a) Lay-out of an OAT imaging system based on a spherical array of sparsely distributed detectors; blue –ultrasound array elements, red –

Accepted Manuscript

light beam, green arrows – scanning direction of the array. (b) Three-dimensional images (top views) of the female breast acquired with the system depicted in (a) [10]. (c) Lay-out of an OAT imaging system based on a Fabry Perot polymer film; blue –ultrasound sensing light beam, red – excitation light beam, green arrows – scanning direction of the sensing beam. (d) Three-dimensional images (top views) of the human fingertip acquired with the system depicted in (c) [143].

In principle, image reconstructions in any of the tomographic imaging systems described above can be performed with the reconstruction algorithms introduced in sections V and VI. Nevertheless, a different class of reconstruction methods worth mentioning is based on the so-called time-reversal approaches [144, 145]. Time-reversal consists in estimating the initial OA pressure by simulating the backward propagation of the US wave with the boundary condition being the measured signals reversed in time. Time-reversal represents a very flexible approach where any acoustic propagation effects can be incorporated into the model. However, those methodologies are typically associated with lengthy reconstruction times, which may hinder applicability in the clinical setting.

VIII. Endoscopic and intravascular optoacoustic imaging

Endoscopic imaging has become a routine part of clinical practice to examine deeply embedded body cavities, e.g. the gastrointestinal, respiratory or urinary tracts. Conventional white light microscopy allows for morphological visualization and is the gold standard in endoscopic procedures. Endoscopic imaging has further evolved to incorporate more sophisticated imaging modalities such as narrow-band imaging, epi-fluorescence, optical coherence tomography (OCT), confocal or two photon microscopy. US endoscopy is also routinely used in the clinics for high resolution imaging at greater depths, yet it lacks the rich functional and molecular contrast of optical imaging. OA can potentially fill those gaps by synergistically combining the advantages of light and sound.

Different OA endoscopic embodiments have been suggested to cover both optical and acoustic resolution regimes. OA endoscopy has been implemented by rotating a light beam and collecting the OA responses with a coaxially aligned US transducer (Fig. 9a). Image formation can be performed analogously to OA microscopy, where the amplitudes of the signals for each scanning position are simply stacked and displayed as cross-sections in polar coordinates (Fig. 9b) [36]. Much like in OA microscopy, endoscopic imaging at depths beyond the diffusive limit of light relies on US beamforming. OA endoscopy can hence be implemented e.g. with single-element focused ultrasound transducers rotated around the probe's axis. By delivering a focused light beam through a cavity in the transducer, optical-resolution images can simultaneously be obtained [38]. Forward looking endoscopes based on Fabry-Perot films have also been developed [146]. In general, overcoming limited-view effects turns particularly challenging in endoscopic OA imaging due to the reduced aperture provided by sensing elements integrated within a relatively small-sized probe. Efforts have been directed towards the development of specifically-designed OA endoscopic probes that maximize the angular coverage around the imaged area. For example, probes based on curved scanning have been suggested. A lay-out of an OA endoscope consisting of a concave array is depicted in Fig 9c [147]. This approach has proven to enhance image quality with respect to that achieved with linear arrays and provide more accurate visualization of vascular structures (Fig. 9d). A different approach to maximize the angular aperture consists in using a flat array covering the entire diameter of the probe and a parabolic mirror to redirect light and ultrasound waves [148]. Alternatively, optimization of the tomographic imaging performance may be achieved by using endoscopic delivery of the excitation light to the tissue of interest while detecting the OA responses from outside the body using an array with large angular coverage [149].

Intravascular imaging is also widely employed in interventional cardiology to characterize the morphology and chemical composition of diseased vessels. Fluorescence, US and OCT are examples of intravascular clinical imaging modalities. Development of intravascular OA is challenged by the need to integrate both light delivery and ultrasound detection elements on a catheter with much smaller diameter than in normal endoscopy. One implementation and representative images are displayed in Figs. 9e and 9f, respectively [150]. Optical fiber light delivery and ultrasound sensors based on Bragg gratings or Fabry Perot resonators have also been suggested for intravascular OA [151]. Optical resolution imaging can be achieved by exploiting directionality of the fiber output. On the other hand, acoustic resolution is challenged by the lack of directionality of the miniaturized US sensors. More importantly, the size-related constrains of the probe prevent the implementation of any tomographic imaging approach unless the generated US waves are detected from outside the body.

Accepted Manuscript

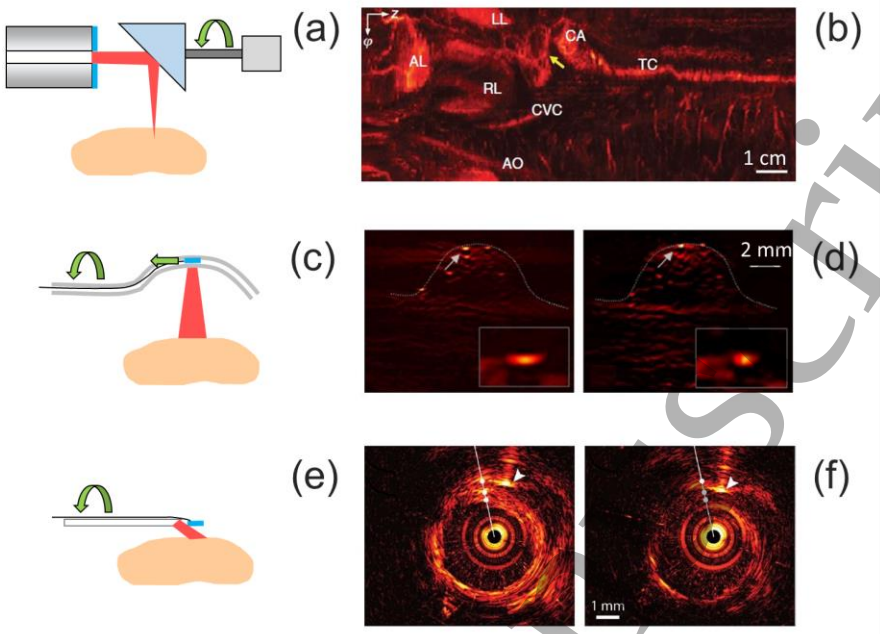


Figure 9: Endoscopic and intravascular optoacoustic (OA) imaging systems. (a) Lay-out of an optical-resolution endoscopic imaging system; blue – sensing surface of the ultrasound transducer, red – light beam; green arrow – circular scanning of the mirror. (b) The corresponding 3D image of a rabbit esophagus acquired with the system [36]. (c) Lay-out of an endoscopic imaging system based on curved scanning; blue – sensing surface of the ultrasound transducer, red – light beam; green arrows – longitudinal scanning of the ultrasound transducer and circular scanning of the endoscope. (d) Cross-sectional images of a mouse tumor obtained with linear (left) versus curved (right) scanning [38]. (e) Lay-out of an intravascular imaging system; blue – sensing surface of the ultrasound transducer, red – light beam; green arrow – circular scanning of the probe. (f) The corresponding intravascular OA images of advanced human atherosclerotic plaques *ex vivo* [150].

IX. Perspective

The unprecedented performance of OA imaging demonstrated in preclinical research is attracting the interest of clinicians in using this technique for diagnostic and treatment monitoring purposes. An increasing number of efforts are being directed into development of new approaches that can facilitate clinical translation. Generally, OA can address any area of the human body located within 1-2 cm from the surface but penetration of up to 5 cm has been reported *in vivo* [22]. Thereby, OA may emerge as a powerful tool in dermatology for the assessment of a large variety of skin lesions, such as melanomas [22, 152, 153], psoriatic patches [23], and non-melanoma skin cancers [154], [155], [156], to name a few representative examples. High-resolution systems further enable visualizing superficial microvascular structures and analyzing microcirculatory changes [92, 130, 157-159]. Angiographic imaging in deeper tissues may further enable assessing atherosclerotic plaques and stenosis in arteries [160], hemorrhages [161] or peripheral arterial disease [24]. Imaging depth is maximized in tissues where light attenuation is less significant, such as the female breast. Thereby, OA breast imaging may emerge as a powerful diagnostic or screening tool, particularly for young women with radiographically dense breasts [10, 133, 141]. Initial clinical trials have shown promise in diagnosis of breast cancer [18, 19, 162], a disease affecting ~8% of women worldwide. Endoscopic systems have further enabled examination of the gastrointestinal tract and other internal organs [163-165]. Intravascular access is also possible, and dedicated probes can find important applications such as the characterization of human coronary atherosclerosis [12, 150, 166, 167]. Potentially important diagnostic feature of the OA method is its high sensitivity to temperature variations as well as ability to spectrally differentiate coagulated tissues, which can be employed for monitoring ablation procedures and other thermal interventions [168-173].

The development of more advanced reconstruction and processing approaches can greatly enhance performance of the existing OA imaging systems in the clinical setting. Of particular importance is the fact that information is displayed in real time to the physician during the procedure. Image rendering has been significantly accelerated with

Accepted Manuscript

GPU-based implementations of reconstruction and processing algorithms [174], which have enabled the visualization of three-dimensional images in real-time [135]. OA reconstruction algorithms can mainly be classified into analytical (e.g. back-projection) [175], model-based (iterative) [118, 176] and time-reversal [177] approaches. In all cases, the mathematical operations can easily be parallelized. More powerful GPUs and more efficient GPU algorithmic implementations are hence essential for the clinical translation of OA imaging. Off-line processing may additionally be performed for a more accurate quantification of clinically relevant bio-markers. Some stationary OA embodiments do not require real-time preview and all processing steps can be performed off-line, e.g. in scanning breast tomography. Advanced reconstruction and processing algorithms can also boost performance by enhancing the spatial resolution [45, 178], improving quantification abilities [179-181] and contrast [137] or providing higher sensitivity in detection of spectrally-distinct substances [182-184]. Recently, machine and deep learning methods have been suggested as a tool to efficiently extract information from OA data [185-187]. Trained neural networks can process complex data in very short time and hence may be used to provide OA real-time feed-back. However, large amounts of good quality data is usually required for proper training, while substantial concerns further exist with respect to error immunity and diagnostic accuracy of those methods.

Despite importance of the reconstruction approaches, improvements in hardware and experimental methodologies are key for achieving optimum OA imaging performance. In comparison with pulse-echo US, the OA images are free of speckle noise [188]. Instead, OA images are afflicted with the so-called limited-view artifacts [68] that hamper visibility of vascular structures, especially in the clinical setting where tomographic access to the region of interest is limited. A potential mitigation strategy consists in incorporating *a priori* knowledge into the reconstructions [189, 190] or using properly trained neural networks [191, 192]. Another promising approach consists of non-linear combination of sequential images containing a sparse and time-varying distribution of optical absorbers. Such source distribution can be achieved e.g. via speckle illumination [193, 194], selective US heating [195] or flowing particles [196, 197]. By determining the position of individual sources, localization OA tomography (LOT) further enables increasing the spatial resolution beyond the acoustic diffraction barrier [198, 199]. For in vivo imaging, this can potentially be achieved by intravenous injection of particulate contrast agents, which would need a separate regulatory approval.

One important aspect that remained outside the scope of this review is the topic of spectral differentiation (un-mixing) in multi-spectral optoacoustic tomography (MSOT) [64, 200]. For instance, haemoglobin in its oxygenated and deoxygenated form is the most dominant intrinsic absorber in mammalian tissues in the visible and most of the NIR spectra, which allows for extraction of useful disease biomarkers. However, accurate determination of distribution of various tissue chromophores and agents by means of MSOT is challenged by the strong wavelength dependence of light attenuation in living tissues. For improving quantitative determination of chromophore concentrations, the light distribution in tissue needs to be accurately accounted for, which represents a challenging problem in OA imaging and tomography [50, 182].

In summary, the great potential of optoacoustic imaging shown in preclinical research has encouraged the translation of this technology into the clinics with multiple applications envisioned, from intraoperative diagnostics to ophthalmology, dermatology, cardiovascular and endoscopic imaging. One of the key advantages of optoacoustic imaging is its intrinsic potential to deliver complete volumetric tomographic datasets from the imaged object with a single interrogating laser pulse, a possibility that does not exist in other clinical imaging modalities. This capacity also comes with important clinical advantages, such as the ability to dynamically visualize the bio-distribution of contrast agents in 3D and reduce out-of-plane and motion artefacts, thus facilitating clinical observations. Despite multiple outstanding technical challenges, development of efficient and accurate image reconstruction approaches is expected to facilitate wide adoption of the OA modality in the clinics.

ACKNOWLEDGMENTS

The authors acknowledge grant support from the European Research Council (ERC-2015-CoG-682379), US National Institute of Health (NIH, R21- EY028365 and UF1-NS107680) and German Research Foundation (DFG, RA1848/5-1).

REFERENCES

Accepted Manuscript

[1] J. Yao, L. Wang, J.-M. Yang, K.I. Maslov, T.T. Wong, L. Li, C.-H. Huang, J. Zou, L.V. Wang, High-speed label-free functional photoacoustic microscopy of mouse brain in action, Nature methods, 12 (2015) 407.
[2] X.L. Deán-Ben, G. Sela, A. Lauri, M. Kneipp, V. Ntziachristos, G.G. Westmeyer, S. Shoham, D. Razansky, Functional optoacoustic neuro-tomography for scalable whole-brain monitoring of calcium indicators, Light: Science & Applications, 5 (2016) e16201.
[3] A.P. Jathoul, J. Laufer, O. Ogunlade, B. Treeby, B. Cox, E. Zhang, P. Johnson, A.R. Pizzey, B. Philip, T. Marafioti, Deep in vivo photoacoustic imaging of mammalian tissues using a tyrosinase-based genetic reporter, Nat Photonics, 9 (2015) 239.
[4] M.R. Tomaszewski, I.Q. Gonzalez, J.P. O'Connor, O. Abeyakoon, G.J. Parker, K.J. Williams, F.J. Gilbert, S.E. Bohndiek, Oxygen enhanced optoacoustic tomography (OE-OT) reveals vascular dynamics in murine models of prostate cancer, Theranostics, 7 (2017) 2900.
[5] J. Reber, M. Willershäuser, A. Karlas, K. Paul-Yuan, G. Diot, D. Franz, T. Fromme, S.V. Ovsepian, N. Bézière, E. Dubikovskaya, Non-invasive measurement of brown fat metabolism based on optoacoustic imaging of hemoglobin gradients, Cell metabolism, 27 (2018) 689-701. e684.
[6] H.-C.A. Lin, X.L. Déan-Ben, I. Ivankovic, M.A. Kimm, K. Kosanke, H. Haas, R. Meier, F. Lohöfer, M. Wildgruber, D. Razansky, Characterization of Cardiac Dynamics in an Acute Myocardial Infarction Model by Four-Dimensional Optoacoustic and Magnetic Resonance Imaging, Theranostics, 7 (2017) 4470.
[7] J. Weber, P.C. Beard, S.E. Bohndiek, Contrast agents for molecular photoacoustic imaging, Nature methods, 13 (2016) 639-650.
[8] M.R. Kelly-Goss, B. Ning, A.C. Bruce, D.N. Tavakol, D. Yi, S. Hu, P.A. Yates, S.M. Peirce, Dynamic, heterogeneous endothelial Tie2 expression and capillary blood flow during microvascular remodeling, Sci Rep-Uk, 7 (2017) 9049.
[9] M. Schwarz, M. Omar, A. Buehler, J. Aguirre, V. Ntziachristos, Implications of ultrasound frequency in optoacoustic mesoscopy of the skin, IEEE transactions on medical imaging, 34 (2015) 672-677.
[10] R.A. Kruger, C.M. Kuzmiak, R.B. Lam, D.R. Reinecke, S.P. Del Rio, D. Steed, Dedicated 3D photoacoustic breast imaging, Medical physics, 40 (2013).
[11] A. Dima, V. Ntziachristos, Non-invasive carotid imaging using optoacoustic tomography, Optics express, 20 (2012) 25044-25057.
[12] K. Jansen, M. Wu, A.F. van der Steen, G. van Soest, Photoacoustic imaging of human coronary atherosclerosis in two spectral bands, Photoacoustics, 2 (2014) 12-20.
[13] J. Zhang, S. Yang, X. Ji, Q. Zhou, D. Xing, Characterization of lipid-rich aortic plaques by intravascular photoacoustic tomography: ex vivo and in vivo validation in a rabbit atherosclerosis model with histologic correlation, J Am Coll Cardiol, 64 (2014) 385-390.
[14] C. Tian, Z. Xie, M.L. Fabiilli, X. Wang, Imaging and sensing based on dual-pulse nonlinear photoacoustic contrast: a preliminary study on fatty liver, Opt Lett, 40 (2015) 2253-2256.
[15] A. Buehler, G. Diot, T. Volz, J. Kohlmeyer, V. Ntziachristos, Imaging of fatty tumors: appearance of subcutaneous lipomas in optoacoustic images, Journal of biophotonics, 10 (2017) 983-989.
[16] X. Li, C.D. Heldermon, L. Yao, L. Xi, H. Jiang, High resolution functional photoacoustic tomography of breast cancer, Medical physics, 42 (2015) 5321-5328.
[17] M. Heijblom, D. Piras, M. Brinkhuis, J.C. van Hespen, F. Van den Engh, M. Van der Schaaf, J. Klaase, T. Van Leeuwen, W. Steenbergen, S. Manohar, Photoacoustic image patterns of breast carcinoma and comparisons with Magnetic Resonance Imaging and vascular stained histopathology, Sci Rep-Uk, 5 (2015) 11778.
[18] G. Diot, S. Metz, A. Noske, E. Liapis, B. Schroeder, S.V. Ovsepian, R. Meier, E.J. Rummeny, V. Ntziachristos, Multi-Spectral Optoacoustic Tomography (MSOT) of human breast cancer, Clin Cancer Res, DOI (2017) clincanres. 3200.2016.
[19] L. Lin, P. Hu, J. Shi, C.M. Appleton, K. Maslov, L. Li, R. Zhang, L.V. Wang, Single-breath-hold photoacoustic computed tomography of the breast, Nat Commun, 9 (2018) 2352.
[20] F. Knieling, C. Neufert, A. Hartmann, J. Claussen, A. Urich, C. Egger, M. Vetter, S. Fischer, L. Pfeifer, A. Hagel, Multispectral optoacoustic tomography for assessment of Crohn's disease activity, New England Journal of Medicine, 376 (2017) 1292-1294.
[21] V.S. Dogra, B.K. Chinni, K.S. Valluru, J. Moalem, E.J. Giampoli, K. Evans, N.A. Rao, Preliminary results of ex vivo multispectral photoacoustic imaging in the management of thyroid cancer, Am J Roentgenol, 202 (2014) W552-W558.
[22] I. Stoffels, S. Morscher, I. Helfrich, U. Hillen, J. Leyh, N.C. Burton, T.C. Sardella, J. Claussen, T.D. Poeppel, H.S. Bachmann, Metastatic status of sentinel lymph nodes in melanoma determined noninvasively with multispectral optoacoustic imaging, Sci Transl Med, 7 (2015) 317ra199-317ra199.

Accepted Manuscript

[23] J. Aguirre, M. Schwarz, N. Garzorz, M. Omar, A. Buehler, K. Eyerich, V. Ntziachristos, Precision assessment of label-free psoriasis biomarkers with ultra-broadband optoacoustic mesoscopy, Nature Biomedical Engineering, 1 (2017) 0068.
[24] A. Taruttis, A.C. Timmermans, P.C. Wouters, M. Kacprowicz, G.M. van Dam, V. Ntziachristos, Optoacoustic imaging of human vasculature: feasibility by using a handheld probe, Radiology, 281 (2016) 256-263.
[25] L. Li, L. Zhu, C. Ma, L. Lin, J. Yao, L. Wang, K. Maslov, R. Zhang, W. Chen, J. Shi, Single-impulse panoramic photoacoustic computed tomography of small-animal whole-body dynamics at high spatiotemporal resolution, Nature biomedical engineering, 1 (2017) 0071.
[26] X.L. Deán-Ben, T.F. Fehm, S.J. Ford, S. Gottschalk, D. Razansky, Spiral volumetric optoacoustic tomography visualizes multi-scale dynamics in mice, Light: Science & Applications, 6 (2017) e16247.
[27] A. Buehler, M. Kacprowicz, A. Taruttis, V. Ntziachristos, Real-time handheld multispectral optoacoustic imaging, Opt Lett, 38 (2013) 1404-1406.
[28] X. Deán-Ben, T.F. Fehm, D. Razansky, Universal hand-held three-dimensional optoacoustic imaging probe for deep tissue human angiography and functional preclinical studies in real time, Journal of visualized experiments: JoVE, DOI (2014).
[29] A. Taruttis, V. Ntziachristos, Advances in real-time multispectral optoacoustic imaging and its applications, Nat Photonics, 9 (2015) 219.
[30] C. Kim, T.N. Erpelding, L. Jankovic, M.D. Pashley, L.V. Wang, Deeply penetrating in vivo photoacoustic imaging using a clinical ultrasound array system, Biomedical optics express, 1 (2010) 278-284.
[31] J. Yuan, G. Xu, Y. Yu, Y. Zhou, P.L. Carson, X. Wang, X. Liu, Real-time photoacoustic and ultrasound dual-modality imaging system facilitated with graphics processing unit and code parallel optimization, Journal of biomedical optics, 18 (2013) 086001.
[32] K. Daoudi, P. Van Den Berg, O. Rabot, A. Kohl, S. Tisserand, P. Brands, W. Steenbergen, Handheld probe integrating laser diode and ultrasound transducer array for ultrasound/photoacoustic dual modality imaging, Optics express, 22 (2014) 26365-26374.
[33] C.-W. Wei, T.-M. Nguyen, J. Xia, B. Arnal, E.Y. Wong, I.M. Pelivanov, M. O'Donnell, Real-time integrated photoacoustic and ultrasound (PAUS) imaging system to guide interventional procedures: ex vivo study, IEEE transactions on ultrasonics, ferroelectrics, and frequency control, 62 (2015) 319-328.
[34] X. Deán-Ben, E. Merčep, D. Razansky, Hybrid-array-based optoacoustic and ultrasound (OPUS) imaging of biological tissues, Appl Phys Lett, 110 (2017) 203703.
[35] A. Rosenthal, S. Kellnberger, D. Bozhko, A. Chekkoury, M. Omar, D. Razansky, V. Ntziachristos, Sensitive interferometric detection of ultrasound for minimally invasive clinical imaging applications, Laser Photonics Rev, 8 (2014) 450-457.
[36] J.-M. Yang, C. Favazza, R. Chen, J. Yao, X. Cai, K. Maslov, Q. Zhou, K.K. Shung, L.V. Wang, Simultaneous functional photoacoustic and ultrasonic endoscopy of internal organs in vivo, Nature medicine, 18 (2012) 1297.
[37] X. Ji, K. Xiong, S. Yang, D. Xing, Intravascular confocal photoacoustic endoscope with dual-element ultrasonic transducer, Optics express, 23 (2015) 9130-9136.
[38] H. He, G. Wissmeyer, S.V. Ovsepian, A. Buehler, V. Ntziachristos, Hybrid optical and acoustic resolution optoacoustic endoscopy, Opt Lett, 41 (2016) 2708-2710.
[39] Y. Yang, X. Li, T. Wang, P.D. Kumavor, A. Aguirre, K.K. Shung, Q. Zhou, M. Sanders, M. Brewer, Q. Zhu, Integrated optical coherence tomography, ultrasound and photoacoustic imaging for ovarian tissue characterization, Biomedical optics express, 2 (2011) 2551-2561.
[40] P. Shao, W. Shi, P.H. Reza, R.J. Zemp, Integrated micro-endoscopy system for simultaneous fluorescence and optical-resolution photoacoustic imaging, Journal of biomedical optics, 17 (2012) 076024.
[41] A. Rosenthal, V. Ntziachristos, D. Razansky, Acoustic inversion in optoacoustic tomography: A review, Curr Med Imaging Rev, 9 (2013) 318-336.
[42] J. Yao, L.V. Wang, Photoacoustic microscopy, Laser Photonics Rev, 7 (2013) 758-778.
[43] K. Wang, S.A. Ermilov, R. Su, H.-P. Brecht, A.A. Oraevsky, M.A. Anastasio, An imaging model incorporating ultrasonic transducer properties for three-dimensional optoacoustic tomography, IEEE transactions on medical imaging, 30 (2011) 203-214.
[44] A. Rosenthal, V. Ntziachristos, D. Razansky, Model-based optoacoustic inversion with arbitrary-shape detectors, Medical physics, 38 (2011) 4285-4295.
[45] D. Queirós, X.L. Déan-Ben, A. Buehler, D. Razansky, A. Rosenthal, V. Ntziachristos, Modeling the shape of cylindrically focused transducers in three-dimensional optoacoustic tomography, Journal of biomedical optics, 18 (2013) 076014.

Accepted Manuscript

[46] J. Jose, R.G. Willemink, W. Steenbergen, C.H. Slump, T.G. van Leeuwen, S. Manohar, Speed-of-sound compensated photoacoustic tomography for accurate imaging, Medical physics, 39 (2012) 7262-7271.
[47] X.L. Deán-Ben, V. Ntziachristos, D. Razansky, Effects of small variations of speed of sound in optoacoustic tomographic imaging, Medical physics, 41 (2014).
[48] G. Wurzinger, R. Nuster, G. Paltauf, Combined photoacoustic, pulse-echo laser ultrasound, and speed-of-sound imaging using integrating optical detection, Journal of biomedical optics, 21 (2016) 086010.
[49] T.P. Matthews, M.A. Anastasio, Joint reconstruction of the initial pressure and speed of sound distributions from combined photoacoustic and ultrasound tomography measurements, Inverse Probl, 33 (2017) 124002.
[50] K. Maslov, H.F. Zhang, L.V. Wang, Effects of wavelength-dependent fluence attenuation on the noninvasive photoacoustic imaging of hemoglobin oxygen saturation in subcutaneous vasculature in vivo, Inverse Probl, 23 (2007) S113.
[51] S. Mandal, X.-L. Dean-Ben, D. Razansky, Visual Quality Enhancement in Optoacoustic Tomography Using Active Contour Segmentation Priors, IEEE Trans. Med. Imaging, 35 (2016) 2209-2217.
[52] Y. Liu, H. Jiang, Z. Yuan, Two schemes for quantitative photoacoustic tomography based on Monte Carlo simulation, Medical physics, 43 (2016) 3987-3997.
[53] V.V. Perekatova, M.Y. Kirillin, I.V. Turchin, P.V. Subochev, Combination of virtual point detector concept and fluence compensation in acoustic resolution photoacoustic microscopy, Journal of biomedical optics, 23 (2018) 091414.
[54] X.L. Deán-Ben, D. Razansky, V. Ntziachristos, The effects of acoustic attenuation in optoacoustic signals, Physics in Medicine & Biology, 56 (2011) 6129.
[55] H. Roitner, P. Burgholzer, Efficient modeling and compensation of ultrasound attenuation losses in photoacoustic imaging, Inverse Probl, 27 (2010) 015003.
[56] B.E. Treeby, Acoustic attenuation compensation in photoacoustic tomography using time-variant filtering, Journal of biomedical optics, 18 (2013) 036008.
[57] X.L. Deán-Ben, V. Ntziachristos, D. Razansky, Artefact reduction in optoacoustic tomographic imaging by estimating the distribution of acoustic scatterers, Journal of biomedical optics, 17 (2012) 110504.
[58] J. Poudel, T.P. Matthews, L. Li, M.A. Anastasio, L.V. Wang, Mitigation of artifacts due to isolated acoustic heterogeneities in photoacoustic computed tomography using a variable data truncation-based reconstruction method, Journal of biomedical optics, 22 (2017) 041018.
[59] X.L. Dean-Ben, A. Ozbek, D. Razansky, Volumetric real-time tracking of peripheral human vasculature with GPU-accelerated three-dimensional optoacoustic tomography, IEEE transactions on medical imaging, 32 (2013) 2050-2055.
[60] American National Standards for the Safe Use of Lasers ANSI Z136.1, American Laser Institute, 2000.
[61] X.L. Deán-Ben, D. Razansky, Functional optoacoustic human angiography with handheld video rate three dimensional scanner, Photoacoustics, 1 (2013) 68-73.
[62] S.L. Jacques, Optical properties of biological tissues: a review, Physics in medicine and biology, 58 (2013) R37-R61.
[63] D. Razansky, Multispectral optoacoustic tomography—Volumetric color hearing in real time, Ieee J Sel Top Quant, 18 (2012) 1234-1243.
[64] B. Cox, J.G. Laufer, S.R. Arridge, P.C. Beard, Quantitative spectroscopic photoacoustic imaging: a review, Journal of biomedical optics, 17 (2012).
[65] Y. Xu, L.V. Wang, G. Ambartsoumian, P. Kuchment, Reconstructions in limited-view thermoacoustic tomography, Medical physics, 31 (2004) 724-733.
[66] G. Paltauf, R. Nuster, M. Haltmeier, P. Burgholzer, Experimental evaluation of reconstruction algorithms for limited view photoacoustic tomography with line detectors, Inverse Probl, 23 (2007) S81.
[67] A. Buehler, A. Rosenthal, T. Jetzfellner, A. Dima, D. Razansky, V. Ntziachristos, Model-based optoacoustic inversions with incomplete projection data, Medical physics, 38 (2011) 1694-1704.
[68] X.L. Deán-Ben, D. Razansky, On the link between the speckle free nature of optoacoustics and visibility of structures in limited-view tomography, Photoacoustics, 4 (2016) 133-140.
[69] W. Dan, T. Chao, L. Xiao-Jun, W. Xue-Ding, Influence of limited-view scanning on depth imaging of photoacoustic tomography, Chinese Phys B, 21 (2012) 014301.
[70] K. Mitsuhashi, J. Poudel, T.P. Matthews, A. Garcia-Uribe, L.V. Wang, M.A. Anastasio, A forward-adjoint operator pair based on the elastic wave equation for use in transcranial photoacoustic computed tomography, SIAM journal on imaging sciences, 10 (2017) 2022-2048.
[71] H.c. Estrada, X. Huang, J. Rebling, M. Zwack, S. Gottschalk, D. Razansky, Virtual craniotomy for high-resolution optoacoustic brain microscopy, Sci Rep-Uk, 8 (2018) 1459.

Accepted Manuscript

[72] X.L. Deán-Ben, R. Ma, A. Rosenthal, V. Ntziachristos, D. Razansky, Weighted model-based optoacoustic reconstruction in acoustic scattering media, Physics in Medicine & Biology, 58 (2013) 5555.
[73] H.N.Y. Nguyen, A. Hussain, W. Steenbergen, Reflection artifact identification in photoacoustic imaging using multi-wavelength excitation, Biomedical optics express, 9 (2018) 4613-4630.
[74] S.L. Jacques, R.D. Glickman, J.A. Schwartz, Internal absorption coefficient and threshold for pulsed laser disruption of melanosomes isolated from retinal pigment epithelium, Laser-Tissue Interaction VII, International Society for Optics and Photonics, 1996, pp. 468-478.
[75] http://omlc.org/spectra, DOI.
[76] G.M. Hale, M.R. Querry, Optical constants of water in the 200-nm to 200-μm wavelength region, Applied optics, 12 (1973) 555-563.
[77] R. Van Veen, H.J. Sterenborg, A. Pifferi, A. Torricelli, E. Chikoidze, R. Cubeddu, Determination of visible near-IR absorption coefficients of mammalian fat using time-and spatially resolved diffuse reflectance and transmission spectroscopy, Journal of biomedical optics, 10 (2005) 054004.
[78] C.-L. Tsai, J.-C. Chen, W.-J. Wang, Near-infrared absorption property of biological soft tissue constituents, Journal of Medical and Biological Engineering, 21 (2001) 7-14.
[79] S.L. Jacques, Optical properties of biological tissues: a review, Physics in Medicine & Biology, 58 (2013) R37.
[80] A.M. Winkler, K.I. Maslov, L.V. Wang, Noise-equivalent sensitivity of photoacoustics, Journal of biomedical optics, 18 (2013) 097003.
[81] X. Deán-Ben, D. Razansky, Optoacoustic signal excitation with a tone-burst of short pulses, Photoacoustics, 11 (2018) 1.
[82] P. Beard, Biomedical photoacoustic imaging, Interface Focus, DOI (2011) rsfs20110028.
[83] L.V. Wang, Tutorial on photoacoustic microscopy and computed tomography, Ieee J Sel Top Quant, 14 (2008) 171-179.
[84] C.G. Hoelen, F.F. de Mul, Image reconstruction for photoacoustic scanning of tissue structures, Applied optics, 39 (2000) 5872-5883.
[85] X. Wang, Y. Pang, G. Ku, X. Xie, G. Stoica, L.V. Wang, Noninvasive laser-induced photoacoustic tomography for structural and functional in vivo imaging of the brain, Nat Biotechnol, 21 (2003) 803.
[86] H.F. Zhang, K. Maslov, G. Stoica, L.V. Wang, Functional photoacoustic microscopy for high-resolution and noninvasive in vivo imaging, Nat Biotechnol, 24 (2006) 848.
[87] H.-P.F. Brecht, R. Su, M.P. Fronheiser, S.A. Ermilov, A. Conjusteau, A.A. Oraevsky, Whole-body three-dimensional optoacoustic tomography system for small animals, Journal of biomedical optics, 14 (2009) 064007.
[88] D. Razansky, A. Buehler, V. Ntziachristos, Volumetric real-time multispectral optoacoustic tomography of biomarkers, Nature protocols, 6 (2011) 1121.
[89] A. Buehler, X. Deán-Ben, J. Claussen, V. Ntziachristos, D. Razansky, Three-dimensional optoacoustic tomography at video rate, Optics express, 20 (2012) 22712-22719.
[90] J. Xia, L.V. Wang, Small-animal whole-body photoacoustic tomography: a review, IEEE Trans. Biomed. Engineering, 61 (2014) 1380-1389.
[91] G. Paltauf, P. Hartmair, G. Kovachev, R. Nuster, Piezoelectric line detector array for photoacoustic tomography, Photoacoustics, 8 (2017) 28-36.
[92] H.-C. Hsu, L. Wang, L.V. Wang, In vivo photoacoustic microscopy of human cuticle microvasculature with single-cell resolution, Journal of biomedical optics, 21 (2016) 056004.
[93] J. Yao, L.V. Wang, Sensitivity of photoacoustic microscopy, Photoacoustics, 2 (2014) 87-101.
[94] C. Tian, W. Zhang, A. Mordovanakis, X. Wang, Y.M. Paulus, Noninvasive chorioretinal imaging in living rabbits using integrated photoacoustic microscopy and optical coherence tomography, Optics express, 25 (2017) 15947-15955.
[95] L.V. Wang, J. Yao, A practical guide to photoacoustic tomography in the life sciences, Nature methods, 13 (2016) 627.
[96] J. Shi, Y. Tang, J. Yao, Advances in super-resolution photoacoustic imaging, Quantitative imaging in medicine and surgery, 8 (2018) 724.
[97] C. Zhang, K.I. Maslov, J. Yao, L.V. Wang, In vivo photoacoustic microscopy with 7.6-μm axial resolution using a commercial 125-MHz ultrasonic transducer, Journal of biomedical optics, 17 (2012) 116016.
[98] W. Liu, Y. Zhou, M. Wang, L. Li, E. Vienneau, R. Chen, J. Luo, C. Xu, Q. Zhou, L.V. Wang, Correcting the limited view in optical-resolution photoacoustic microscopy, Journal of biophotonics, 11 (2018) e201700196.
[99] S. Park, C. Lee, J. Kim, C. Kim, Acoustic resolution photoacoustic microscopy, Biomedical Engineering Letters, 4 (2014) 213-222.

Accepted Manuscript

[100] E.M. Strohm, M.J. Moore, M.C. Kolios, High resolution ultrasound and photoacoustic imaging of single cells, Photoacoustics, 4 (2016) 36-42.
[101] M. Schwarz, J. Aguirre, M. Omar, V. Ntziachristos, Optoacoustic Imaging of Skin, Imaging in Dermatology, Elsevier2016, pp. 375-385.
[102] C.P. Favazza, L.V. Wang, O.W. Jassim, L.A. Cornelius, In vivo photoacoustic microscopy of human cutaneous microvasculature and a nevus, Journal of biomedical optics, 16 (2011) 016015.
[103] M.-L. Li, H.F. Zhang, K. Maslov, G. Stoica, L.V. Wang, Improved in vivo photoacoustic microscopy based on a virtual-detector concept, Opt Lett, 31 (2006) 474-476.
[104] J. Turner, H. Estrada, M. Kneipp, D. Razansky, Improved optoacoustic microscopy through three-dimensional spatial impulse response synthetic aperture focusing technique, Opt Lett, 39 (2014) 3390-3393.
[105] J. Park, S. Jeon, J. Meng, L. Song, J.S. Lee, C. Kim, Delay-multiply-and-sum-based synthetic aperture focusing in photoacoustic microscopy, Journal of biomedical optics, 21 (2016) 036010.
[106] M.Á.A. Caballero, A. Rosenthal, J. Gateau, D. Razansky, V. Ntziachristos, Model-based optoacoustic imaging using focused detector scanning, Opt Lett, 37 (2012) 4080-4082.
[107] S. Bu, Z. Liu, T. Shiina, K. Kondo, M. Yamakawa, K. Fukutani, Y. Someda, Y. Asao, Model-based reconstruction integrated with fluence compensation for photoacoustic tomography, Ieee T Bio-Med Eng, 59 (2012) 1354-1363.
[108] X.L. Deán-Ben, H. Estrada, M. Kneipp, J. Turner, D. Razansky, Three-dimensional modeling of the transducer shape in acoustic resolution optoacoustic microscopy, Photons Plus Ultrasound: Imaging and Sensing 2014, International Society for Optics and Photonics, 2014, pp. 89434V.
[109] K. Sivasubramanian, M. Pramanik, High frame rate photoacoustic imaging at 7000 frames per second using clinical ultrasound system, Biomedical optics express, 7 (2016) 312-323.
[110] A. Hariri, J. Lemaster, J. Wang, A.S. Jeevarathinam, D.L. Chao, J.V. Jokerst, The characterization of an economic and portable LED-based photoacoustic imaging system to facilitate molecular imaging, Photoacoustics, 9 (2018) 10-20.
[111] Y. Zhu, G. Xu, J. Yuan, J. Jo, G. Gandikota, H. Demirci, T. Agano, N. Sato, Y. Shigeta, X. Wang, Light Emitting Diodes based Photoacoustic Imaging and Potential Clinical Applications, Sci Rep-Uk, 8 (2018) 9885.
[112] Y. Wang, R.S.A. Lim, H. Zhang, N. Nyayapathi, K.W. Oh, J. Xia, Optimizing the light delivery of linear-array-based photoacoustic systems by double acoustic reflectors, Sci Rep-Uk, 8 (2018) 13004.
[113] J. Kim, S. Park, Y. Jung, S. Chang, J. Park, Y. Zhang, J.F. Lovell, C. Kim, Programmable real-time clinical photoacoustic and ultrasound imaging system, Sci Rep-Uk, 6 (2016) 35137.
[114] M.P. Fronheiser, S.A. Ermilov, H.-P.F. Brecht, A. Conjusteau, R. Su, K. Mehta, A.A. Oraevsky, Real-time optoacoustic monitoring and three-dimensional mapping of a human arm vasculature, Journal of biomedical optics, 15 (2010) 021305.
[115] D. Wang, Y. Wang, Y. Zhou, J.F. Lovell, J. Xia, Coherent-weighted three-dimensional image reconstruction in linear-array-based photoacoustic tomography, Biomedical optics express, 7 (2016) 1957-1965.
[116] S. Preisser, G. Held, H.G. Akarçay, M. Jaeger, M. Frenz, Study of clutter origin in in-vivo epi-optoacoustic imaging of human forearms, J Optics-Uk, 18 (2016) 094003.
[117] M.W. Schellenberg, H.K. Hunt, Hand-held optoacoustic imaging: A review, Photoacoustics, DOI (2018).
[118] A. Rosenthal, D. Razansky, V. Ntziachristos, Fast semi-analytical model-based acoustic inversion for quantitative optoacoustic tomography, IEEE transactions on medical imaging, 29 (2010) 1275-1285.
[119] X.L. Dean-Ben, V. Ntziachristos, D. Razansky, Acceleration of optoacoustic model-based reconstruction using angular image discretization, IEEE transactions on medical imaging, 31 (2012) 1154-1162.
[120] A. Rosenthal, T. Jetzfellner, D. Razansky, V. Ntziachristos, Efficient framework for model-based tomographic image reconstruction using wavelet packets, IEEE transactions on medical imaging, 31 (2012) 1346-1357.
[121] C. Lutzweiler, X.L. Deán-Ben, D. Razansky, Expediting model-based optoacoustic reconstructions with tomographic symmetries, Medical physics, 41 (2014).
[122] T. Jetzfellner, A. Rosenthal, K.-H. Englmeier, A. Dima, M.Á.A. Caballero, D. Razansky, V. Ntziachristos, Interpolated model-matrix optoacoustic tomography of the mouse brain, Appl Phys Lett, 98 (2011) 163701.
[123] L. Ding, X.L. Deán-Ben, D. Razansky, Real-time model-based inversion in cross-sectional optoacoustic tomography, IEEE transactions on medical imaging, 35 (2016) 1883-1891.
[124] E. Mercep, G. Jeng, S. Morscher, P.-C. Li, D. Razansky, Hybrid optoacoustic tomography and pulse-echo ultrasonography using concave arrays, IEEE transactions on ultrasonics, ferroelectrics, and frequency control, 62 (2015) 1651-1661.
[125] E. Merčep, X.L. Deán-Ben, D. Razansky, Combined pulse-echo ultrasound and multispectral optoacoustic tomography with a multi-segment detector array, IEEE transactions on medical imaging, 36 (2017) 2129-2137.

Accepted Manuscript

[126] E. Merčep, X.L. Deán-Ben, D. Razansky, Imaging of blood flow and oxygen state with a multi-segment optoacoustic ultrasound array, Photoacoustics, 10 (2018) 48-53.
[127] L. Xiang, B. Wang, L. Ji, H. Jiang, 4-D photoacoustic tomography, Sci Rep-Uk, 3 (2013) 1113.
[128] X.L. Deán-Ben, D. Razansky, Portable spherical array probe for volumetric real-time optoacoustic imaging at centimeter-scale depths, Optics express, 21 (2013) 28062-28071.
[129] R. Nagaoka, T. Tabata, S. Yoshizawa, S.-i. Umemura, Y. Saijo, Visualization of murine lymph vessels using photoacoustic imaging with contrast agents, Photoacoustics, 9 (2018) 39-48.
[130] X.L. Deán-Ben, H. López-Schier, D. Razansky, Optoacoustic micro-tomography at 100 volumes per second, Sci Rep-Uk, 7 (2017) 6850.
[131] X.L. Deán-Ben, D. Razansky, Adding fifth dimension to optoacoustic imaging: volumetric time-resolved spectrally enriched tomography, Light: Science & Applications, 3 (2014) e137.
[132] S. Gottschalk, T. Felix Fehm, X. Luís Deán-Ben, D. Razansky, Noninvasive real-time visualization of multiple cerebral hemodynamic parameters in whole mouse brains using five-dimensional optoacoustic tomography, Journal of Cerebral Blood Flow & Metabolism, 35 (2015) 531-535.
[133] X.L. Deán-Ben, T.F. Fehm, M. Gostic, D. Razansky, Volumetric hand-held optoacoustic angiography as a tool for real-time screening of dense breast, Journal of biophotonics, 9 (2016) 253-259.
[134] Y. Matsumoto, Y. Asao, A. Yoshikawa, H. Sekiguchi, M. Takada, M. Furu, S. Saito, M. Kataoka, H. Abe, T. Yagi, Label-free photoacoustic imaging of human palmar vessels: a structural morphological analysis, Sci Rep-Uk, 8 (2018) 786.
[135] A. Ozbek, X. Deán-Ben, D. Razansky, Realtime parallel back-projection algorithm for three-dimensional optoacoustic imaging devices, European Conference on Biomedical Optics, Optical Society of America, 2013, pp. 88000I.
[136] X.L. Deán-Ben, A. Özbek, D. Razansky, Accounting for speed of sound variations in volumetric hand-held optoacoustic imaging, Frontiers of Optoelectronics, 10 (2017) 280-286.
[137] L. Ding, X.L. Deán-Ben, D. Razansky, Efficient 3-D model-based reconstruction scheme for arbitrary optoacoustic acquisition geometries, IEEE transactions on medical imaging, 36 (2017) 1858-1867.
[138] T.F. Fehm, X.L. Deán-Ben, D. Razansky, Four dimensional hybrid ultrasound and optoacoustic imaging via passive element optical excitation in a hand-held probe, Appl Phys Lett, 105 (2014) 173505.
[139] A. Dima, N.C. Burton, V. Ntziachristos, Multispectral optoacoustic tomography at 64, 128, and 256 channels, Journal of biomedical optics, 19 (2014) 036021.
[140] T.F. Fehm, X.L. Deán-Ben, S.J. Ford, D. Razansky, In vivo whole-body optoacoustic scanner with real-time volumetric imaging capacity, Optica, 3 (2016) 1153-1159.
[141] M. Heijblom, D. Piras, F.M. van den Engh, M. van der Schaaf, J.M. Klaase, W. Steenbergen, S. Manohar, The state of the art in breast imaging using the Twente Photoacoustic Mammoscope: results from 31 measurements on malignancies, European radiology, 26 (2016) 3874-3887.
[142] S.A. Ermilov, T. Khamapirad, A. Conjusteau, M.H. Leonard, R. Lacewell, K. Mehta, T. Miller, A.A. Oraevsky, Laser optoacoustic imaging system for detection of breast cancer, Journal of biomedical optics, 14 (2009) 024007.
[143] A.A. Plumb, N.T. Huynh, J. Guggenheim, E. Zhang, P. Beard, Rapid volumetric photoacoustic tomographic imaging with a Fabry-Perot ultrasound sensor depicts peripheral arteries and microvascular vasomotor responses to thermal stimuli, European radiology, 28 (2018) 1037-1045.
[144] Y. Hristova, P. Kuchment, L. Nguyen, Reconstruction and time reversal in thermoacoustic tomography in acoustically homogeneous and inhomogeneous media, Inverse Probl, 24 (2008) 055006.
[145] B.E. Treeby, B.T. Cox, k-Wave: MATLAB toolbox for the simulation and reconstruction of photoacoustic wave fields, Journal of biomedical optics, 15 (2010) 021314.
[146] R. Ansari, E.Z. Zhang, A.E. Desjardins, P.C. Beard, All-optical forward-viewing photoacoustic probe for high-resolution 3D endoscopy, Light: Science & Applications, 7 (2018) 75.
[147] H. He, A. Buehler, V. Ntziachristos, Optoacoustic endoscopy with curved scanning, Opt Lett, 40 (2015) 4667-4670.
[148] D. Tsyboulski, A. Conjusteau, A. Oraevsky, Dual modality optoacoustic and laser ultrasound endoscopy system, Photons Plus Ultrasound: Imaging and Sensing 2014, International Society for Optics and Photonics, 2014, pp. 89432S.
[149] P. Kruizinga, A.F. van der Steen, N. de Jong, G. Springeling, J.L. Robertus, A. van der Lugt, G. van Soest, Photoacoustic imaging of carotid artery atherosclerosis, Journal of biomedical optics, 19 (2014) 110504.
[150] K. Jansen, A.F. Van Der Steen, H.M. van Beusekom, J.W. Oosterhuis, G. van Soest, Intravascular photoacoustic imaging of human coronary atherosclerosis, Opt Lett, 36 (2011) 597-599.

Accepted Manuscript

[151] E.Z. Zhang, P.C. Beard, A miniature all-optical photoacoustic imaging probe, Photons plus ultrasound: imaging and sensing 2011, International Society for Optics and Photonics, 2011, pp. 78991F.
[152] Y. Zhou, G. Li, L. Zhu, C. Li, L.A. Cornelius, L.V. Wang, Handheld photoacoustic probe to detect both melanoma depth and volume at high speed in vivo, Journal of biophotonics, 8 (2015) 961-967.
[153] S. Mallidi, G.P. Luke, S. Emelianov, Photoacoustic imaging in cancer detection, diagnosis, and treatment guidance, Trends Biotechnol, 29 (2011) 213-221.
[154] S.Y. Chuah, A.B.E. Attia, C.J.H. Ho, X. Li, J.S.-S. Lee, M.W.P. Tan, A.A. Yong, A.W.M. Tan, D. Razansky, M. Olivo, Volumetric Multispectral Optoacoustic Tomography for 3-Dimensional Reconstruction of Skin Tumors: A Further Evaluation with Histopathologic Correlation, J Invest Dermatol, 139 (2019) 481-485.
[155] A.B.E. Attia, S.Y. Chuah, D. Razansky, C.J.H. Ho, P. Malempati, U. Dinish, R. Bi, C.Y. Fu, S.J. Ford, J.S.-S. Lee, Noninvasive real-time characterization of non-melanoma skin cancers with handheld optoacoustic probes, Photoacoustics, 7 (2017) 20-26.
[156] S. Chuah, A. Attia, V. Long, C. Ho, P. Malempati, C. Fu, S. Ford, J. Lee, W. Tan, D. Razansky, Structural and functional 3D mapping of skin tumours with non-invasive multispectral optoacoustic tomography, Skin Research and Technology, 23 (2017) 221-226.
[157] D. Xu, S. Yang, Y. Wang, Y. Gu, D. Xing, Noninvasive and high-resolving photoacoustic dermoscopy of human skin, Biomedical optics express, 7 (2016) 2095-2102.
[158] M. Schwarz, A. Buehler, J. Aguirre, V. Ntziachristos, Three-dimensional multispectral optoacoustic mesoscopy reveals melanin and blood oxygenation in human skin in vivo, Journal of biophotonics, 9 (2016) 55-60.
[159] P. Subochev, A. Orlova, E. Smolina, A. Kirillov, N. Shakhova, I. Turchin, Raster-scan optoacoustic angiography reveals 3D microcirculatory changes during cuffed occlusion, Laser Phys Lett, 15 (2018) 045602.
[160] I. Ivankovic, Real-Time Volumetric Assessment of the Human Carotid Artery: Handheld Multispectral Optoacoustic Tomography, Radiology (in press), DOI.
[161] D. Wu, J. Yang, G. Zhang, H. Jiang, Noninvasive in vivo monitoring of collagenase induced intracerebral hemorrhage by photoacoustic tomography, Biomedical optics express, 8 (2017) 2276-2286.
[162] M. Heijblom, W. Steenbergen, S. Manohar, Clinical photoacoustic breast imaging: the twente experience, Ieee Pulse, 6 (2015) 42-46.
[163] S. Tang, J. Chen, P. Samant, K. Stratton, L. Xiang, Transurethral photoacoustic endoscopy for prostate cancer: a simulation study, IEEE transactions on medical imaging, 35 (2016) 1780-1787.
[164] Y. Qu, C. Li, J. Shi, R. Chen, S. Xu, H. Rafsanjani, K. Maslov, H. Krigman, L. Garvey, P. Hu, Transvaginal fast-scanning optical-resolution photoacoustic endoscopy, Journal of biomedical optics, 23 (2018) 121617.
[165] T.-J. Yoon, Y.-S. Cho, Recent advances in photoacoustic endoscopy, World journal of gastrointestinal endoscopy, 5 (2013) 534.
[166] B. Wang, J.L. Su, J. Amirian, S.H. Litovsky, R. Smalling, S. Emelianov, Detection of lipid in atherosclerotic vessels using ultrasound-guided spectroscopic intravascular photoacoustic imaging, Optics express, 18 (2010) 4889-4897.
[167] P. Wang, T. Ma, M.N. Slipchenko, S. Liang, J. Hui, K.K. Shung, S. Roy, M. Sturek, Q. Zhou, Z. Chen, High-speed intravascular photoacoustic imaging of lipid-laden atherosclerotic plaque enabled by a 2-kHz barium nitrite raman laser, Sci Rep-Uk, 4 (2014) 6889.
[168] S. Iskander-Rizk, P. Kruizinga, A.F. van der Steen, G. van Soest, Spectroscopic photoacoustic imaging of radiofrequency ablation in the left atrium, Biomedical optics express, 9 (2018) 1309-1322.
[169] J. Rebling, F.J.O. Landa, X.L. Deán-Ben, A. Douplik, D. Razansky, Integrated catheter for simultaneous radio frequency ablation and optoacoustic monitoring of lesion progression, Opt Lett, 43 (2018) 1886-1889.
[170] E. Petrova, H. Brecht, M. Motamedi, A. Oraevsky, S. Ermilov, In vivo optoacoustic temperature imaging for image-guided cryotherapy of prostate cancer, Physics in Medicine & Biology, 63 (2018) 064002.
[171] F.J.O. Landa, X.L. Deán-Ben, R. Sroka, D. Razansky, Volumetric optoacoustic temperature mapping in photothermal therapy, Sci Rep-Uk, 7 (2017) 9695.
[172] F.J.O. Landa, S.R. Penacoba, F.M. de Espinosa, D. Razansky, X.L. Deán-Ben, Four-dimensional optoacoustic monitoring of tissue heating with medium intensity focused ultrasound, Ultrasonics, DOI (2018).
[173] J. Gray, N. Dana, K. Dextraze, F. Maier, S. Emelianov, R. Bouchard, Multi-wavelength photoacoustic visualization of high intensity focused ultrasound lesions, Ultrasonic Imaging, 38 (2016) 96-112.
[174] G. Pratx, L. Xing, GPU computing in medical physics: A review, Medical physics, 38 (2011) 2685-2697.
[175] M. Xu, L.V. Wang, Universal back-projection algorithm for photoacoustic computed tomography, Phys Rev E, 71 (2005) 016706.
[176] K. Wang, R. Su, A.A. Oraevsky, M.A. Anastasio, Investigation of iterative image reconstruction in three-dimensional optoacoustic tomography, Physics in Medicine & Biology, 57 (2012) 5399.

Accepted Manuscript

[177] B.E. Treeby, E.Z. Zhang, B.T. Cox, Photoacoustic tomography in absorbing acoustic media using time reversal, Inverse Probl, 26 (2010) 115003.
[178] K. Mitsuhashi, K. Wang, M.A. Anastasio, Investigation of the far-field approximation for modeling a transducer's spatial impulse response in photoacoustic computed tomography, Photoacoustics, 2 (2014) 21-32.
[179] L. Ding, X.L. Deán-Ben, C. Lutzweiler, D. Razansky, V. Ntziachristos, Efficient non-negative constrained model-based inversion in optoacoustic tomography, Physics in Medicine & Biology, 60 (2015) 6733.
[180] G. Balasundaram, L. Ding, X. Li, A.B.E. Attia, X.L. Dean-Ben, C.J.H. Ho, P. Chandrasekharan, H.C. Tay, H.Q. Lim, C.B. Ong, Noninvasive Anatomical and Functional Imaging of Orthotopic Glioblastoma Development and Therapy using Multispectral Optoacoustic Tomography, Translational oncology, 11 (2018) 1251-1258.
[181] B.T. Cox, J.G. Laufer, P.C. Beard, S.R. Arridge, Quantitative spectroscopic photoacoustic imaging: a review, Journal of biomedical optics, 17 (2012) 061202.
[182] S. Tzoumas, A. Nunes, I. Olefir, S. Stangl, P. Symvoulidis, S. Glasl, C. Bayer, G. Multhoff, V. Ntziachristos, Eigenspectra optoacoustic tomography achieves quantitative blood oxygenation imaging deep in tissues, Nat Commun, 7 (2016) ncomms12121.
[183] L. Ding, X.L. Deán-Ben, N.C. Burton, R.W. Sobol, V. Ntziachristos, D. Razansky, Constrained Inversion and Spectral Unmixing in Multispectral Optoacoustic Tomography, IEEE transactions on medical imaging, 36 (2017) 1676-1685.
[184] S. Tzoumas, N. Deliolanis, S. Morscher, V. Ntziachristos, Unmixing molecular agents from absorbing tissue in multispectral optoacoustic tomography, IEEE transactions on medical imaging, 33 (2014) 48-60.
[185] S. Antholzer, M. Haltmeier, J. Schwab, Deep learning for photoacoustic tomography from sparse data, Inverse Problems in Science and Engineering, DOI (2018) 1-19.
[186] D. Allman, A. Reiter, M.A.L. Bell, Photoacoustic Source Detection and Reflection Artifact Removal Enabled by Deep Learning, IEEE transactions on medical imaging, 37 (2018) 1464-1477.
[187] A. Hauptmann, B. Cox, F. Lucka, N. Huynh, M. Betcke, P. Beard, S. Arridge, Approximate k-space models and Deep Learning for fast photoacoustic reconstruction, International Workshop on Machine Learning for Medical Image Reconstruction, Springer, 2018, pp. 103-111.
[188] Z. Guo, L. Li, L.V. Wang, On the speckle-free nature of photoacoustic tomography, Medical physics, 36 (2009) 4084-4088.
[189] T. Oruganti, J.G. Laufer, B.E. Treeby, Vessel filtering of photoacoustic images, Photons Plus Ultrasound: Imaging and Sensing 2013, International Society for Optics and Photonics, 2013, pp. 85811W.
[190] Y. Han, L. Ding, X.L.D. Ben, D. Razansky, J. Prakash, V. Ntziachristos, Three-dimensional optoacoustic reconstruction using fast sparse representation, Opt Lett, 42 (2017) 979-982.
[191] A. Hauptmann, F. Lucka, M. Betcke, N. Huynh, J. Adler, B. Cox, P. Beard, S. Ourselin, S. Arridge, Model-Based Learning for Accelerated, Limited-View 3-D Photoacoustic Tomography, IEEE transactions on medical imaging, 37 (2018) 1382-1393.
[192] D. Waibel, J. Gröhl, F. Isensee, T. Kirchner, K. Maier-Hein, L. Maier-Hein, Reconstruction of initial pressure from limited view photoacoustic images using deep learning, Photons Plus Ultrasound: Imaging and Sensing 2018, International Society for Optics and Photonics, 2018, pp. 104942S.
[193] J. Gateau, T. Chaigne, O. Katz, S. Gigan, E. Bossy, Improving visibility in photoacoustic imaging using dynamic speckle illumination, Opt Lett, 38 (2013) 5188-5191.
[194] T. Chaigne, J. Gateau, M. Allain, O. Katz, S. Gigan, A. Sentenac, E. Bossy, Super-resolution photoacoustic fluctuation imaging with multiple speckle illumination, Optica, 3 (2016) 54-57.
[195] L. Wang, G. Li, J. Xia, L.V. Wang, Ultrasonic-heating-encoded photoacoustic tomography with virtually augmented detection view, Optica, 2 (2015) 307-312.
[196] X.L. Deán-Ben, L. Ding, D. Razansky, Dynamic particle enhancement in limited-view optoacoustic tomography, Opt Lett, 42 (2017) 827-830.
[197] T. Chaigne, B. Arnal, S. Vilov, E. Bossy, O. Katz, Super-resolution photoacoustic imaging via flow-induced absorption fluctuations, Optica, 4 (2017) 1397-1404.
[198] X.L. Dean-Ben, D. Razansky, Localization optoacoustic tomography, Light: Science & Applications, 7 (2018) 18004.
[199] S. Vilov, B. Arnal, E. Bossy, Overcoming the acoustic diffraction limit in photoacoustic imaging by the localization of flowing absorbers, Opt Lett, 42 (2017) 4379-4382.
[200] F.M. Brochu, J. Brunker, J. Joseph, M.R. Tomaszewski, S. Morscher, S.E. Bohndiek, Towards quantitative evaluation of tissue absorption coefficients using light fluence correction in optoacoustic tomography, IEEE transactions on medical imaging, 36 (2017) 322-331.

Accepted Manuscript